

AUTOMATIC QUANTIFICATION FROM CT SCANS OF MORPHOLOGICAL
CHANGES IN PULMONARY ARTERIAL VASCULATURE IN PULMONARY ARTERY
HYPERTENSION

By

ANKIT SALGIA

A THESIS PRESENTED TO THE GRADUATE SCHOOL
OF THE UNIVERSITY OF FLORIDA IN PARTIAL FULFILLMENT
OF THE REQUIREMENTS FOR THE DEGREE OF
MASTER OF SCIENCE

UNIVERSITY OF FLORIDA

2012

© 2012 Ankit Salgia

“To my mother Lata Salgia – She is the reason why I am here”

ACKNOWLEDGMENTS

I wish to thank all those who helped in different ways through graduate school. I would like to begin by expressing my sincere gratitude to Dr. Walter G. O'Dell, my thesis advisor and mentor. His motivation and guidance through these years at the laboratory, in addition to his enthusiasm and humor, have made working with him an educational and enjoyable experience. I would also like to thank my committee members, Dr. Hans Van Oostrom for his suggestions and ideas, and Dr. Paul Richard Carney for his motivation and cheerful suggestions during various stages of this work.

I would like to extend my gratitude to Dr. R. James White for his suggestions, motivation and insightful discussions during online meetings. Specially, I would like to thank him for providing data sets needed in this study. It was a great opportunity to work with him.

My time as a graduate research assistant at the lab was filled with fun, joy and learning, thanks to my fellow colleague Siddharth Ray, and the independent reader on my thesis project, Rujuta D. Munje. I would also like to acknowledge my friends, Sonam Chheda, Anoop Thomas Joy, Joshua Hopkins, Lee Ravid, Tammy Banh, and Sathvik Lakshminarayan, for sharing some great times during graduate school. Special thanks go to Pratik Salgia for his support, and for sharing great stories that were both insightful and entertaining.

I wish to extend my sincere gratitude Tifiny D. McDonald for administrative and friendly support during various occasions. I am deeply indebted to the support and kindness my parents have shown me during stressful and happy times. I extend my thanks to my dad and mom for being the wonderful understanding parents they are.

Finally, I wish to thank my funding from the Shands Cancer Centre, University of Florida.

TABLE OF CONTENTS

	<u>page</u>
ACKNOWLEDGMENTS.....	4
LIST OF FIGURES.....	9
ABSTRACT	11
CHAPTER	
1 INTRODUCTION	13
1.1 Objective.....	13
1.2 Motivation	14
1.2.1 Clinical Motivation	14
1.2.2 Research Significance.....	15
1.2.3 Overview of Planned Work.....	15
1.3 Hypothesis and Specific Aims.....	17
1.4 Organization of the Report.....	17
2 BACKGROUND AND RELEVANT WORK.....	19
2.1 Vessel Extraction Techniques.....	19
2.1.1 Mathematical Morphological Schemes	19
2.1.2 Skeleton-Based Approach.....	20
2.1.3 Region Growing Methods.....	22
2.2 Morphology Extraction Techniques.....	22
2.2.1 Fast Marching Method.....	23
2.2.2 Euclidean Distance Transform	24
2.3 Selection Criteria for the Current Task.....	24
2.3.1 Extraction and Segmentation of Lung Vessel.....	25
2.3.1.1 Morphological operations to extract lung volume from human/phantom-CT	26
2.3.1.2 Seeded region growing algorithm to segment the pulmonary vasculature	28
2.3.2 Morphology Extraction of Lung Vessel	30
3 MATERIALS AND METHODS	36
3.1 Materials	36
3.1.1 Anthropomorphic Phantom Data Set.....	36
3.1.2 Micro-CT Rat Data Set	37
3.2 Methods.....	38
3.2.1 Automated Segmentation of Pulmonary Vasculature in the Anthropomorphic Phantom.....	38
3.2.1.1 Initial processing of DICOM/TIFF image files.....	39

3.2.1.2	Extraction of lung volume.....	39
3.2.1.3	Initialization of seed points.....	40
3.2.1.4	Initialization of timestamp.....	40
3.2.1.5	Voxel selection and segmentation.....	40
3.2.1.6	Morphology extraction.....	40
3.2.2	Outline of the Fast-marching Algorithm.....	45
3.3	Matlab Function.....	46
3.4	Validation and Analysis for the Automated Tool.....	46
3.4.1	Validation Data Sets.....	47
3.4.2	Validation Results.....	57
4	RESULTS.....	58
4.1	Anthropomorphic Phantom Lung CT Segmentation and Morphology Extraction.....	58
4.1.1	Extraction of Lung Volume.....	58
4.1.2	Initialization of Starting Seed Point.....	58
4.1.3	Voxel Selection and Segmentation.....	59
4.1.4	Morphology Extraction.....	59
4.2	Micro-CT Rat Lung Segmentation and Morphology Extraction.....	63
4.2.1	Initialization of Starting Seed Point.....	63
4.2.2	Voxel Selection and Segmentation.....	65
4.2.3	Morphology Extraction.....	66
5	DISCUSSION.....	73
5.1	Time Stamp.....	74
5.2	Wavefront Radius.....	74
6	CONCLUSION AND FUTURE WORK.....	75
6.1	Conclusion.....	75
6.2	Limitations and Future Work.....	75
	REFERENCES.....	77
	BIOGRAPHICAL SKETCH.....	80

LIST OF TABLES

<u>Table</u>		<u>page</u>
3-1	Shows the radius obtained by the independent reader computed manually and obtained by my tool.	50
3-2	Results compared with the ground truth obtained from the independent reader and results obtained from the tool.	56
4-1	Comparison between different metrics of vessel morphology to distinguish changes in vascular tree size	62
4-2	Correlation coefficient calculated between different metrics of vessel morphology in anthropomorphic phantom data sets.	62
4.3	Comparison between different metrics of vessel morphology in healthy and PAH rat lungs	71
4-4	Correlation coefficient calculated between different metrics of vessel morphology in rat data sets.	71

LIST OF FIGURES

<u>Figure</u>	<u>page</u>
1-1 Ixolaris(Ixo) preserves vascular structure and density in rats with established PAH.....	16
2-1 Centerline obtained using skeleton based method in a 2D phantom.....	21
2-2 Lung volume extraction using the method of Wang et al. on a representative slice from a CT data set of an anthropomorphic thoracic chest phantom	28
2-3 Grid point updating in 3D.....	32
2-4 Initialize seed point and starting of Fast Marching Method.....	33
2-5 Updating process of Fast Marching Method in 2D.....	33
2-6 Overview of propagation of fast marching across 2D grid	34
3.1 Exterior Shell of Thoracic Platform and Vasculature Phantom	36
3-2 Representative 2D,axial CT images showing a cross-sectional slice of the 3Dimage data set of the anthropomorphic chest phantom.	39
3-3 The first synthetic data set (#1) used to test the semi-automated vessel tree extraction software	49
3-4 The second synthetic data set (#2) used to test the semi-automated vessel tree extraction software.	51
3-5 The third synthetic data set (#3) used to test the semi-automated vessel tree extraction software.	53
3-6 The fourth synthetic data set (#4) used to test the semi-automated vessel tree extraction software, cuboid model 3D image volume.	53
3-7 The fifth synthetic data set (#5) used to test the semi-automated vessel tree extraction software, cuboid model 3D image volume.	54
3-8 The sixth synthetic data set (#6) used to test the semi-automated vessel tree extraction software	54
3-9 The seventh synthetic data set (#7) used to test the semi-automated vessel tree extraction software.	55
4-1 A CT image slice #80 in the anthropomorphic phantom showing seed point selection	59

4-2	Results of the vessel tree segmentation in the anthropomorphic phantom CT...	60
4-3	3D rendering of intermediate steps in morphology extraction of the anthropomorphic Phantom Data set.	61
4-4	Shows Multiple Seed Point Selections (white arrows) in the 3D lung volume of a diseased rat lung data set.....	64
4-5	Seed Point Selection in two different rat data sets..	64
4-6	Shows results of the segmentation of rat lung vasculature.....	66
4-7	Histogram of radius of branch on log scale with standard deviation.	67
4-8	Histogram of length of branches on log scale with standard deviation..	68
4-9	Histogram of branch tortuosity on log scale with standard deviation.	68
4-10	Histogram of branch angle on log scale with standard deviation.	69
4-11	Histogram of the ratio of branch length over branch radius.	70
4-12	shows the linear fit between Normalized lung area and Lung Volume.	72

Abstract of Thesis Presented to the Graduate School
of the University of Florida in Partial Fulfillment of the
Requirements for the Degree of Master of Science

AUTOMATIC QUANTIFICATION FROM CT SCANS OF MORPHOLOGICAL
CHANGES IN PULMONARY ARTERIAL VASCULATURE IN PULMONARY ARTERY
HYPERTENSION

By

Ankit Salgia

May 2012

Chair: Walter G O'Dell
Major: Biomedical Engineering

Pulmonary Arterial Hypertension (PAH) occurs in an idiopathic form and is also associated with diseases such as congenital heart malformation, scleroderma, HIV infection, and cirrhosis. Severe PAH is rare but has a dismal prognosis: even contemporary therapy provides only a 75% three-year survival as found in a recent consecutive cohort of patients followed from 1994-2002.

In PAH, small and medium arterioles are progressively occluded by vascular and inflammatory cells. Better, more convenient therapies are needed and such therapeutic advances will require a more thorough understanding of vascular remodeling, right ventricular (RV) compensation, and RV failure. The current methods of studying this disease are not very quantitative. The quantitative extraction of morphology features of the lung pulmonary vasculature is important for the diagnosis of the extent or progression of PAH. This work will help to identify/quantify key biomarkers of disease progression and the efficacy of the emerging drugs used for therapy. The purpose of this thesis work is to develop automated extraction of pulmonary vascular tree features

from 3D computed tomography (CT) images and to quantify/identify morphological changes of the vasculature tree in PAH in rats with hopes to subsequently apply it to humans. In brief, the task begins by identifying and labeling each vessel branch/bifurcation point. Following centerline extraction, the number of descending segments, number of branches, distribution of branch radii, mean branch radius, distribution of branch lengths, mean branch length, branch angle and tortuosity are computed, along with overall vascular volume, spatial fractal dimension and normalized lung area. Together, these parameters are referred to as the metrics of vessel morphology.

I have used a seeded region growing method that performs the initial vessel tree segmentation, and a fast marching method that performs morphological extraction of the metrics of vessel morphology. The algorithm was developed and validated on synthetic data sets and on scans of an anthropomorphic lung phantom. To measure the performance of the algorithm, the results were compared to a ground truth database obtained manually by an independent reader.

In a representative healthy rat lung, over 9,000 branches were extracted, labeled and characterized. The PAH-diseased lung was found to have large, measurable differences in the metrics of vessel morphology compared with controls.

CHAPTER 1 INTRODUCTION

According to the French registry, the prevalence of pulmonary arterial hypertension (PAH) is about 15 per million, while previously it was considered as rare disease [1]. The World Health Organization (WHO) has classified pulmonary hypertension (PH) into five categories, one of them is PAH. Further, PAH is classified into three sub categories 1) idiopathic pulmonary arterial hypertension (IPAH), 2) familial pulmonary arterial hypertension (FPAH), and 3) pulmonary arterial hypertension related to risk factors or associated conditions (APAH). These PAH categories includes both primary and secondary hypertension[2].

In PAH, small and medium arterioles are progressively occluded by vascular and inflammatory cells. The progressive loss of the pulmonary circulation increases vascular resistance; simultaneously, medial hypertrophy and inflammation in patent vessels reduces compliance, and the combination of decreased compliance and increased resistance dramatically increases right ventricular (RV) afterload. Individual patients display a heterogeneous response to similar degrees of increased RV afterload, with some patients evolving reasonably compensated RV hypertrophy and others quickly decompensating towards RV failure and death. The different RV responses to the same mechanical loads suggest that additional factors of the diseased pulmonary circulation also directly impair RV function in many patients.

1.1 Objective

The overall objective of this work is to quantify changes in pulmonary vasculature structure during pulmonary arterial hypertension as a means to improve our understanding of the biological and mechanical underpinning of PAH and as a metric for

assessing the efficacy of emerging treatments. The specific aim of this thesis project is to develop an automated computational tool to perform the segmentation and extraction of the pulmonary vasculature, and to determine metrics of vessel morphology for distinguishing different stages of pulmonary arterial hypertension disease compared with healthy controls. The hypothesis is that at least one of these metrics of vessel morphology can be used to reliably quantify the extent of PAH disease in a rat model.

1.2 Motivation

1.2.1 Clinical Motivation

PAH usually occurs in idiopathic form (IPAH) and is also associated with diseases such as congenital heart malformation, scleroderma, HIV infection, and cirrhosis (APAH)[3]. Severe PAH is rare: only 2–3 incidence per million per year[4]. For reasons not understood, females are 3 times more likely than males to get PAH [5]. Severe PAH has a dismal prognosis. Patients generally die from decompensated right ventricular (RV) failure and contemporary therapy provides only a 75% three-year survival, as evident in a recent study of patients followed from 1994-2002 [6]. Many patients require lung transplantation. Pulmonary vascular findings at autopsy include neointimal formation and obliteration of the arteriole lumen. Better, more convenient therapies are needed [7], [8] and such therapeutic advances will require a more thorough understanding of vascular remodeling. There are currently no objective approaches to measure the extent of pulmonary vascular disease in patients with PAH. For better understanding of the disease, we need an enhanced means to analyze the underlying morphological changes, which can give better insight into disease progression.

1.2.2 Research Significance

More effective treatment approaches and agents are being developed for the treatment of PAH. Such agents include small molecule inhibitors of tissue factor and thrombin, as recently presented by our colleagues at the University of Rochester [3]. In addition, improved animal models of PAH have recently been developed. The combined use of pneumonectomy (removal of a hemi-lung) and the endothelial toxin monocrotaline (MCT) [3] applied to rats (Pneum/MCT) induces moderate and severe PAH similar to that seen in PAH patients. In a recent study conducted by our colleagues, volumetric micro-CT scans of excised rat lungs were acquired in healthy controls and rats with Pneum/MCT induced PAH. From the images, it is evident that PAH is associated with a loss in a large number of small and medium sized vessels compared with controls (shown in Figure1-1). PAH-induced rats treated with Ixolaris (Ixo) [11], an anti-thrombin agent, appear to have a greater number of branches compared with PAH-induced rats without any therapy. These observations suggest that the characterization of lung vascular morphology is a viable biomarker of the severity of PAH and efficacy of treatment. Of particular importance are changes in the number of smaller vessels. Current approaches to quantifying vascular morphology involve manual delineation and counting of tree branches.

1.2.3 Overview of Planned Work

In this work, I have developed an automated algorithm for segmentation and extraction of pulmonary blood vessels and metrics of morphological changes in the vasculature structure in PAH. In CT data sets there is often present large background noise and it can be difficult to distinguish between fluids (edema), other tissues and the edges of the vessels of interest, which can cause the region-growing algorithm to move

into undesirable region, referred to as leakage. Moreover, the intensity difference between tissue of interest and surrounding tissue can become nearly indistinguishable for small diameter vessels. So, the approach I proposed to use for the initial vessel tree segmentation is seeded region growing (SRG) using adaptive intensity measures.

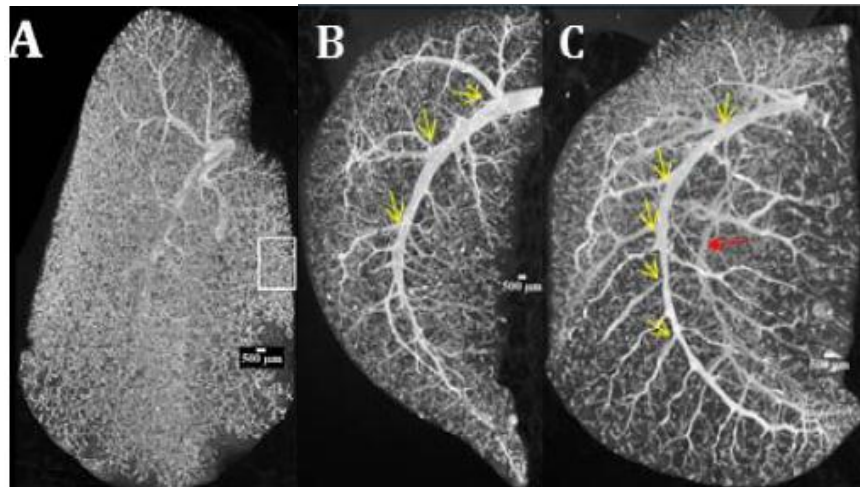


Figure 1-1. Ixolaris (Ixo) preserves vascular structure and density in Pneum/MCT rats with established PAH. [A] Shows normal rat lungs with a large number of smaller vessels. [B] The lung of a Pneum/MCT rat giving only saline for therapy shows extensive pruning of major vessels, as indicated by the yellow arrows, and only one central vessel. [C] The lung of an Ixo-treated Pneum/MCT rat has more large branches, indicated by the yellow arrows, and a second central vessel, indicated by the red arrow.

To quantify/identify metrics of vascular morphology, I proposed to use a fast marching algorithm with wavefront propagation to traverse the vascular tree, and a region-growing method for finding branch bifurcations and labeling each branch. Following a vessel centerline extraction, the number of descending segments, number of branches, distribution of branch radii, mean branch radius, distribution of branch lengths, mean branch length, mean branch angle and tortuosity are computed, along with the overall vascular volume, spatial fractal dimension and normalized lung area. In this thesis, these parameters are referred to as the metrics of vessel morphology. The

aim is to minimize human intervention and effort, and to better quantify the pulmonary vascular morphology.

The algorithm was developed and tested initially on virtual phantoms, and was subsequently tested on X-ray computed tomography (CT) scans of an anthropomorphic lung phantom. Both 2D and 3D virtual phantoms are used to validate the outcomes. Finally, the algorithm was applied to micro-CT scans of excised rat lungs with or without experimentally induced PAH. To assess the performance of the algorithm, the results were compared to a ground truth database obtained manually by an independent reader.

1.3 Hypothesis and Specific Aims

My hypothesis is that the developed algorithm can quantify metrics of vessel morphology that can be used to establish the extent of progression of pulmonary arterial hypertension. The project goals can be divided into three specific aims:

i) Implement the fast marching algorithm and the region-growing algorithm to extract the lung morphology on synthetic and an anthropomorphic lung phantom CT data set.

ii) Validate the algorithm by comparing it with a ground truth and optimize parameters to implement the algorithm on micro-CT images acquired from normal and PAH rat models.

ii) Implement the algorithm to extract the metrics of vessel morphology to evaluate the extent of disease progression.

1.4 Organization of the Report

The remainder of this thesis is organized as follows:

Chapter 2 contains a review of the existing blood vessel extraction and morphology extraction algorithms. It contains the traditional seeded region-growing algorithm and the fast marching algorithm followed by a description of the Euclidean Distance and selection criteria for the current task. Chapter 3 discusses the materials and the methods used in the project. It describes individually the way each specific aim was implemented. Chapter 4 lists the results obtained from the lung segmentation and morphological extraction of the anthropomorphic phantom data sets. It also contains a comparison between normal and PAH rat data sets. Chapter 5 explains some of the assumptions made and concerns addressed during the design of the algorithm, and an analysis of the results obtained. Chapter 6 summarizes the thesis, details the broad application of this work, and discusses possible improvements and potential future work.

CHAPTER 2 BACKGROUND AND RELEVANT WORK

Segmentation of blood vessels has a number of practical applications in medical imaging, including diagnosis of vascular disease and registration of patient images obtained at different times or using different modalities. Vessel segmentation algorithms are used extensively to aid in surgical planning, to visualize vascular deformities and in Computer-Aided Diagnosis (CAD) systems. Knowledge of vessel morphology can be used in the diagnosis of vasculature disease to determine the extent of disease progression [12]. Computer-assisted extraction of vessel morphometry can dramatically decrease the analysis time but by how much depends upon the degree of interaction between the tool and the user. Also, automated vessel tree extraction techniques vary depending on the imaging modality, the organ(s) being imaged, and other factors specific for the clinical task at hand.

Several approaches have been used for vessel segmentation and morphometry extraction. The methods mainly used for X-ray computed tomography (CT) images are: mathematical morphology schemes [13], fast marching algorithms [14] skeleton-based centerline detection methods[15], the vector field method [16] and region growing methods[17]. In the next section each category is discussed with examples presented from the literature.

2.1 Vessel Extraction Techniques

2.1.1 Mathematical Morphological Schemes

Mathematical morphological operators are one of the key components in extraction and enhancement of shape and features. They can also be used with other methods for segmentation of objects. The morphological structuring element used can

be of any shape and form, determined by the geometry to be extracted or enhanced from the object.

Mathematical operators are also often used to fill 'holes' and/or remove unnecessary objects in an image. Erosion and dilation are the basic morphological operators that are most commonly used. Erosion shrinks objects by removing pixels at the object boundaries, and dilation expands objects by adding pixels at the object boundaries, thereby filling holes in binary images.

When erosion and dilation are used in series and with the same structuring element, erosion followed by dilation, bright objects smaller than the size of the structuring element are removed and the remaining objects have their original size and shape restored by the dilation step. The erosion and dilation operations can also be used for vessel segmentation. When the size of structuring element is smaller than the desired vessel, it can be used to remove the surrounding noise. In 2D and 3D images, respectively, the preferred structuring elements are a symmetric disk and a sphere. The successive application of erosion followed by dilation is defined as the morphological operation of image opening. Dilation followed by erosion is defined as image closing and is commonly used to smooth contours and fuse narrow breaks in connectivity.

Pisupati *et al.* [13] demonstrated a method for vessel segmentation using circular structuring elements of several sizes for grayscale opening and opening reconstruction operators to obtain maxima and minima.

2.1.2 Skeleton-Based Approach

Skeleton-based algorithms are used to detect the centerline of each vessel and the vasculature structure is subsequently created by connecting the centerlines. In general, approaches to extract the centerline are based on graph descriptions

containing information about the shape and features of vessel centerlines, thresholding followed by connectivity analysis and thresholding followed by thinning method. A graph description is a list of attributes describing the length of edges in the graph (which relates the strength of similarity of connectedness between graph vertices) and geometric features of each vertex, such as edge point, branch point, and point on loop.

As a representative example of skeleton-base approaches, the approach implemented by Tozaki *et al.* [18] for segmenting blood vessels in thin-slice CT images of the lung is presented. The images were segmented using a threshold and the structures were classified as bronchi or blood vessels based on the property that bronchi contain air on the inside that appears darker in CT images than the heart or blood vessels. Connectivity analysis was performed on the vessel centerlines extracted using 3D thinning. Niki *et al.*[15] used a graph description of curvilinear structures to segment blood vessels in digital angiograms and to analyze their morphology. Their

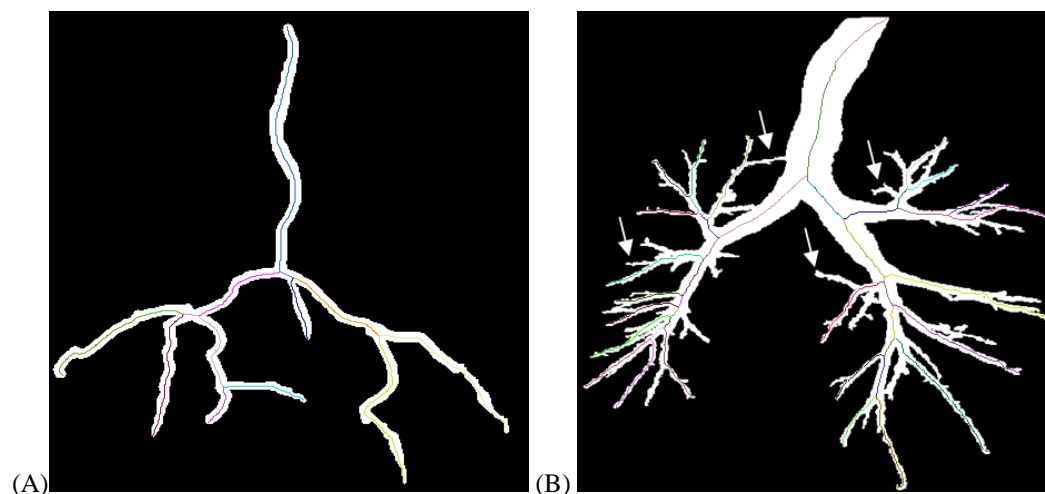


Figure 2-1. Centerline obtained using a skeleton-based method applied to a 2D binary image phantom. [A] The left image shows a simple 2D phantom in which all vessel centerlines are extracted. [B] The right image shows a complex phantom in which several smaller vessels are missed, as indicated by the four white arrows.

procedure consisted of thresholding the images, identifying the maximum connected structure having most pixels and 3D thinning.

The skeleton-based centerline extraction method works good for simple structure where all vessels are of approximately the same radius. But for complex structures where vessel radius reduces on every generation, this method may miss smaller vessels. Representative results are shown in Figure (2.1).

2.1.3 Region Growing Methods

Region growing methods are based on the postulate that pixels within a region have similar appearance features, including intensity and texture. Starting from a seed location, the region is grown by incrementally adding neighboring pixels based on a predefined similarity criterion (for example, a range of acceptable gray-scale values). One or more seeds may be required, depending on the complexity and connectedness of the regions to be segmented.

A classic example of the region growing method is provided by Higgins *et al.* [17] who applied automatic arterial tree extraction to 3D coronary angiograms generated via the fast, high-resolution X-ray CT scanner known as the Dynamic Spatial Reconstructor (DSR). In their technique, the images were first filtered to reduce noise, followed by thresholding and connected-component analysis. A straight-forward seeded region growing method was applied as the final step to extract the vessel trees.

2.2 Morphology Extraction Techniques

Morphology extraction is important in any diseased vasculature structure in order to understand the function of system because morphometry is related to function. Thus, the changes in morphometry help in identifying disease progression and the function

impaired. As, morphological change correlates with changes in pressure in vessel, changes in resistance of vessel and afterload [19].

Wischgoll *et al.* [16] presented a simple image-based method to extract morphometry (diameters, length, and angles) of coronary arteries from knowledge of the vessel centerlines. The centerline extraction algorithm was based on a topological analysis of a vector field generated by normal vectors of the extracted vessel wall. Using a trilinear interpolation, a vector field is created pointing inward to the center of the vessel from the boundaries and the points on the centerlines are computed using a topological analysis of the vector field within the cross-sectional area of the vessel. The individual centerline points are then connected based on the topology of the tetrahedrization. This method gives the sub-voxel representation of the vessel boundary. The vessel length was defined as the length of the centerline and the vessel radius along the centerline was given by the distance between the centerline and the vessel wall. The bifurcation angle was calculated between the centerlines of the segment leads out of the main vessel formed the parent vessel and the larger daughter branch. In addition, they extracted relationships between different parameters based on the centerline and the geometric configuration of the vessel boundary. Their algorithm first extracts the lung volume from the volumetric CT images.

2.2.1 Fast Marching Method

The fast marching method is based on continuous front propagation method and was developed for discrete systems, such as images, which have only integer-valued elements. This method is used for finding out the time taken to reach from one point to another. The front propagation is directed by the following principle: Let $v(p)$ designate the speed function associated with each image point p , and p_0 the starting seed point

(at time zero). Suppose T is the time needed to travel along any given path C between p and p_0 in the image and the travel time along the path can be calculated by the line integral over $v^{-1}(p)$ along C . The time-stamp $U(p)$ is the minimum time taken by the wavefront to reach p among all possible paths between p_0 and p .

$$U(p) = \inf_{C_{p_0,p}} \int_{p_0}^p [v(C(s))]^{-1} ds \dots \dots \dots (2.1)$$

Lorenz *et al.* [14] presented the equation of $U(p)$ given in 2.1 for continuous system. The form for a discrete system is given by the discrete eikonal equation, which is explained in section 2.3.2.

$$U(p) = |\nabla U| = v^{-1} \dots \dots \dots (2.2)$$

2.2.2 Euclidean Distance Transform

The Euclidean distance is defined as the shortest distance between two points as given by the Pythagorean Theorem. A Euclidean distance transform is used in my calculation of the tortuosity of the vessel, as explained in detail in section 3.2.1.6.

2.3 Selection Criteria for the Current Task

In this section, the afore-mentioned vasculature segmentation techniques are evaluated based on our specific goal – which is to segment the vessel tree and extract the morphometry of blood vessels in 3D lung micro-CT images and validated with 3D phantom CT images. The algorithm should be fully automatic or semi-automatic with minimal user interference. The approach needs to be robust to noise, i.e. be able to segment smaller vessels in the presence of moderate to high levels of noise that are typical of lung CT images. In pulmonary arterial hypertension the smaller and the medium size arterioles are primarily affected. The algorithm should be able to detect vessels of small size; as low as 1 mm in radius in human CT data sets and 100-500

microns in radius in rat micro-CT data sets. To summarize, the ideal approach will be simple, fast, semi-automatic, robust to noise, and capable of detecting vasculature structures of small shapes and sizes.

Centerline-based segmentation techniques do not need specific manual initialization and can maintain complex tree structures well. However, they are very sensitive to noise, which makes segmentation of tiny vessels difficult in the presence of noise.

Morphology-based techniques have the valuable feature that they do not require user initialization. However, morphological operators focus on the shape of objects and not on the tree structure and this can result in less accurate results, especially in disease where the vessel geometry can be highly variable.

Fast marching and region growing approaches are based solely on spatial proximity and pixel similarity. Hence, they can be used to segment the blood vessels and the extract the morphometry. It will be further demonstrated in this report that for extracting the vascular tree structure implementation of Seeded Region Growing requires minimal preprocessing and no post-processing. Based on these performance characteristics and the specific requirements of this project, a combination of region-growing and fast-marching approaches were pursued.

2.3.1 Extraction and Segmentation of Lung Vessel

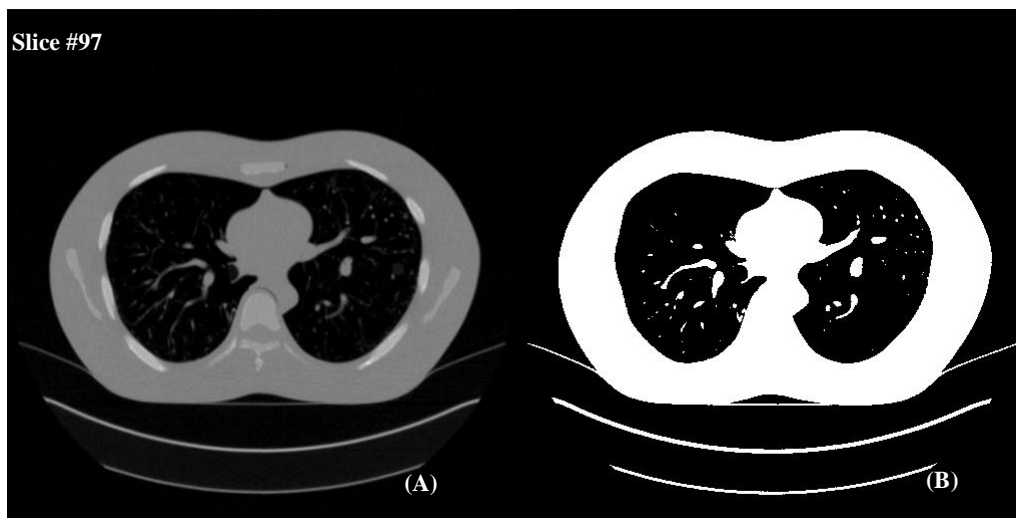
Sindhuja T. Govindarajana (a former student from Dr. O'Dell's laboratory) developed a semi-automated vessel tree extraction algorithm that was tailored for the task of identifying the vessel architecture in with the presence of lung fibrosis [20]. For my thesis work, for the initial task of segmenting the vascular tree, I implemented

previously-developed methods of Wang *et al.*[21] to extract the lung volume and then implemented and optimized the method of Govindarajan *et al.* [20].

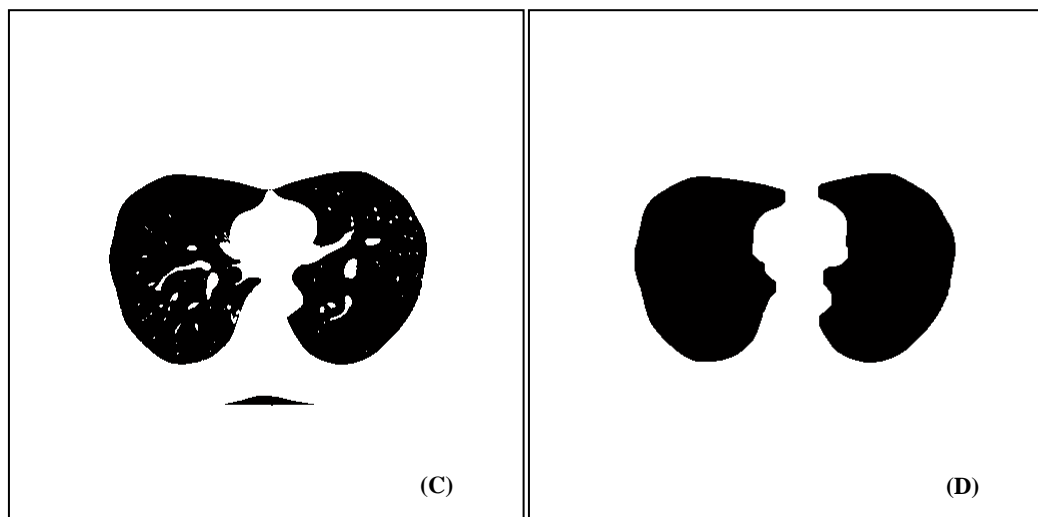
2.3.1.1 Morphological operations to extract lung volume from human/phantom-CT

The micro-CT data sets in PAH and control rats were obtained on excised lungs. No additional processing was needed, therefore, to extract the volume of the lung from the chest wall and other structures present in an intact specimen. In human CT scans and anthropomorphic phantom CT data sets, the following four steps were used to extract the lung volume from the surrounding structures. First, gray-scale intensity thresholding was performed on each 2D gray-scale image in the stack of images that comprise the 3D lung image volume. The threshold level was calculated by using the MATLAB global threshold method to remove initial noise. To create the final lung volume mask, morphological operations were performed such that the lung air space and air external to the body was set to black (binary 0) while the chest wall, heart, liver, arms, pulmonary vessels, etc. were white (binary 1). Morphological opening and closing operations were performed using a disk-shaped structuring element with a radius of 10 pixels. Bright objects in each image slice that were smaller than the size of the structuring element were removed in this process yielding the lung wall mask. Second, a flood-fill operation was applied to the outside of the body. The exterior, air-filled space around the body now became white (binary 1) while the lung air space remained black (binary 0). Third, a morphological opening operation using a disk-shaped structuring element with a radius of 10 pixels was performed to remove objects smaller than this disk size from the internal lung volume. Fourth, A dilation operation was performed using a disk-shaped structuring element of radius 2 pixels to remove any edge effects of the chest wall from being included as part of the lung space. This step helps in the

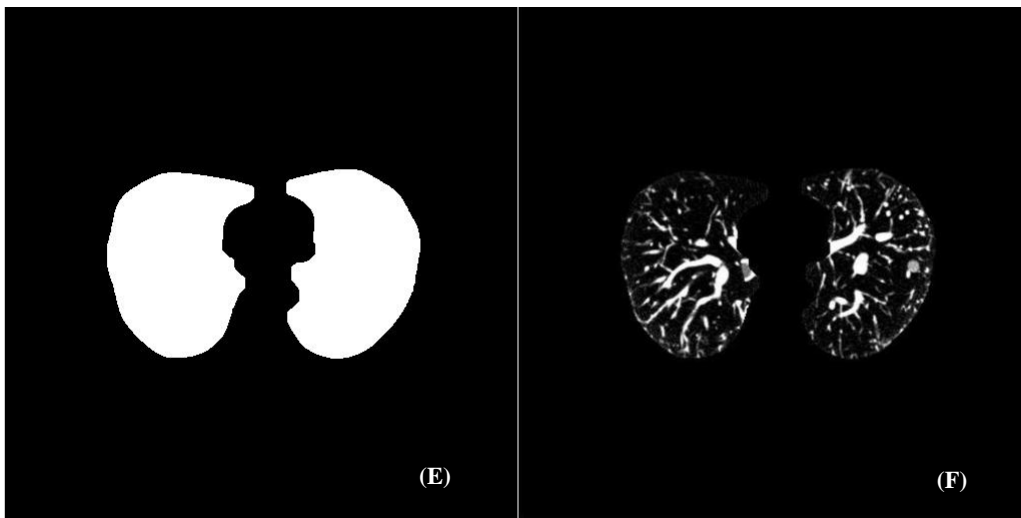
subsequent vessel segmentation steps by preventing the program from mislabeling the residual chest wall as a small vessel and tracing around the lung perimeter. Fifth, gray-scale inversion of the resultant binary image was performed to create the final lung mask where in the lung space (including all interior vessels) was white and all else (chest wall, mediastinum, exterior air space, etc.) was black. Finally, the lung space



In [A] is shown a representative 2D axial slice of the original anthropomorphic phantom CT data set. In [B] is shown the resulting binary image following gray-scale thresholding.



In [C] is shown the binary image following flood-filling of the space external to the body. In [D] is shown the slice after morphological opening operation was performed on [C] to remove smaller sized objects inside the lung volume



In [E] is shown the lung volume mask created by intensity-inverting [D]. Image [F] shows the isolated lung volume after applying the mask in [E] to the original gray-scale image in [A] (The contrast was adjusted here for visual clarity).

Figure2-2. Lung volume extraction using the method of Wang et al on a representative slice from a CT data set of an anthropomorphic thoracic chest phantom.

mask was applied on the original gray-scale images to obtain the inner lung volume.

Figure 2.2 shows the lung volume extraction on a representative slice from a phantom data set.

2.3.1.2 Seeded region growing algorithm to segment the pulmonary vasculature

Seeded region growing (SRG) [23] methods segment an image into regions with respect to a set of user-provided seed points and criteria for similarity and connectivity. The seeds mark each of the connected objects to be segmented. The number of seeds depends on the features of interest, and the presence of noise in the image and the connectedness of the objects of interest. In 3D medical images, the regions are grown iteratively by comparing all unallocated neighboring voxels to the currently labeled region. If the similarity criterion is satisfied, the compared voxel is said to belong to the region. The criteria often used are gray-scale intensity, variance, texture, and shape. The speed of the algorithm depends on the initial seed selection, the number of voxels in the 3D image volume, and the criterion for terminating the recursive allocation of voxels.

In this project, the difference between a voxel's gray-scale intensity value in Hounsfield units and the current, labeled region's mean gray-scale intensity value, $\bar{\delta}$, was used as the measure of similarity. An upper value of $\bar{\delta}$ was provided based on our prior knowledge of the anatomical features of blood vessels in a typical clinical thoracic CT image, acquired without contrast. The voxel with the smallest difference measured this way was allocated to the respective, labeled region. This process continued until either all eligible voxels were allocated to the labeled region or $\bar{\delta}$ exceeded the maximum permissible value.

$\bar{\delta}(x,y,z)$ is a measure of how different a point (x,y,z) is from the region it adjoins and is computed via:

$$\bar{\delta}(x,y,z) = g(x,y,z) - \text{mean}[g(\text{region})]$$

where $g(x,y,z)$ is the gray-scale intensity of the image point (x,y,z) . The region proliferated from a manually selected seed point using region growing, and the difference in gray-scale intensity between the seed voxel and each of six neighboring voxels was computed. The neighboring voxel with intensity closest to that of the region mean was added to the region, and was labeled as the next seed. In the first iteration, the region mean is the same as seed point intensity. The intensity difference between this voxel and the seed was assigned to the variable ($\bar{\delta}$). In addition, all neighboring voxels that had intensities above that of the seed voxel were also added to the region, as the objects with brighter intensity in the lung volume are also of interest. The maximum permissible value for difference ($\bar{\delta}$) between the average intensity of the growing region and the gray-scale intensity of a newly added voxel was chosen based on *a priori* knowledge of the intensity variations between lung tissue, blood vessels and

surrounding air. After the first iteration, the region mean was updated with the average voxel intensity computed in previous step. At each step, the intensity values of all neighboring voxels were compared to the region mean, and the voxel with the closest intensity value was picked as the next seed. The iterative algorithm continued until the new value of \bar{d} was greater than the predefined maximum intensity difference, or the number of included voxels exceeded a predefined maximum voxel count.[23].

Furthermore, if point (x,y,z) is located between two or more regions it is labeled as a boundary voxel and appended to the set of already known boundary voxels. This process is repeated until all connected voxels have been evaluated.

2.3.2 Morphology Extraction of Lung Vessel

The fast marching method is based on front propagation satisfying the eikonal equation. The wavefront propagates away from the seed location in a 3D dome shape and all the points along the front are connected to each other, except where separations occur at vessel branches. I have use the separation of the wavefront at branches to determine the location of bifurcations in the vascular tree. The fast marching algorithm is used simultaneously for traversing the vascular tree and for identifying the centerline of the vasculature structure. In addition to the segmentation, each voxel is labeled with the distance from seed point along the propagating wave, using the quadratic eikonal equation. This information is used later to determine the length and radius of each vessel branch.

Fast Marching Method: Fast marching is the approach used in this thesis work and it was assumed that the path speed of propagation $v(p)$ along path C is constant, i.e. $v(p) = dC/ds = 1$. A constant speed can also be interpreted as meaning that the

distance between two consecutive voxel is 1 unit and the time required to reach to from one voxel to next voxel is one second.

The main idea of the fast marching algorithm is to find the time-stamp (U) on a discrete grid, given by discretized eikonal equation 2.3. This algorithm is used to produce the solution U methodically by front propagation and the fast marching algorithm propagates by updating the search neighborhood in 3D. The solution of the equation for $U(p)$ involves solving a second order partial differential equation (PDE) and the fast marching algorithm makes use of the causality of the front propagation to solve these, in contrast to iterative methods. Here the image is considered as a 2D grid and a stack of images as 3D grid where each grid point corresponds to voxel in the image or image stack. Consider a point in a 3D grid and its six closest neighbors as shown in Figure 2-3. Assume that the neighboring timestamp values are known. The grid point $U_{i,j,k}$ solution is determined by using the discretized eikonal equation.

In the fast marching method each voxel is marked as either *far*, *trial* or *alive*, depending on the region in which it lies. *Far* voxels are those that are not yet reached by the front. *Trial* voxels are those for which a time-stamp has been computed, and *alive* voxels are those trial voxels for which six adjacent voxels has been computed and time stamp has been calculated. Initially all the voxels are labeled as *far* except for one or more seed points which are labeled *trial* and get the time stamp $U_0 = 0$ as shown in Figure 2-4. The marching or front propagation starts from a user defined seed voxel. In Figure 2-4, the black sphere (point p) signifies the origin (seed voxel) or where the U is known [$U(p)=U_0=0$] and the other grid points (remaining voxels) where solution U is unknown. Here it is assume that, the voxel spacing along all coordinate axes of

Euclidean coordinate system is same, for isotropic sampling. Marching progresses outward from U_0 with a new time-stamp $U(p)$ values computed at the six adjacent voxels and called *trial* voxels. Marching continues onto the smallest $U(p)$ value among the *trial* voxels. The smallest valued-point is made *alive* (black sphere in figure 2.4) and its six adjacent points are added to the *trial* voxel group. The $U(p)$ values are updated for each *trial* voxels, as depicted schematically on a 2D grid in Figure 2-5. At each iteration, the smallest timestamp $U(p)$ from the *trial* voxel group is taken for calculating the time-stamp at its six adjacent voxels and this voxel is marked as being among the *alive* voxels. In the fast marching algorithm the information propagates from smaller to larger values of U and mimics the physical process of a wavefront propagation, as shown in Figure 2-6.

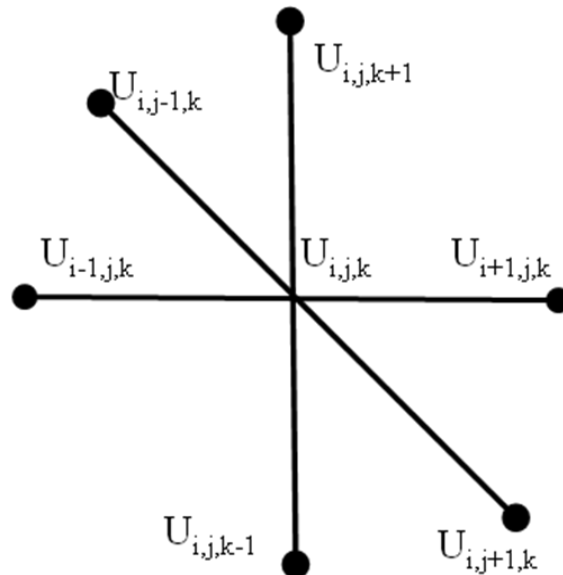


Figure 2-3. Grid point updating in 3D

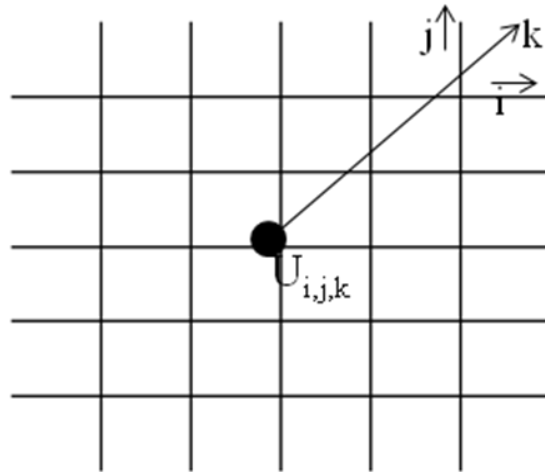
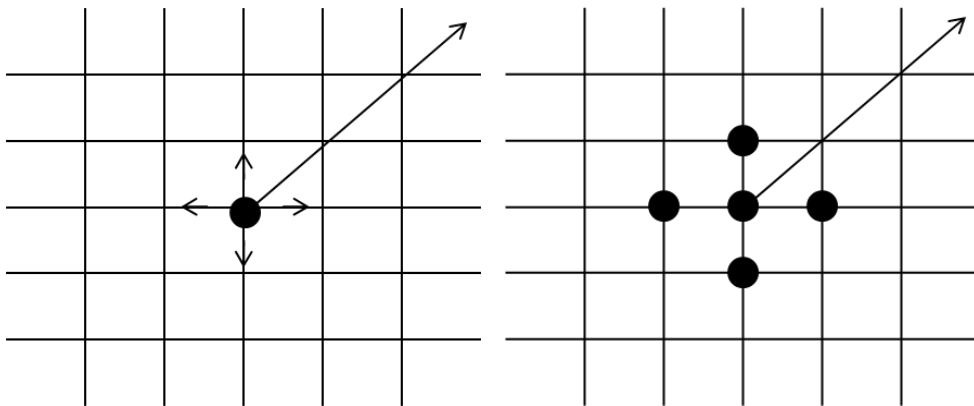
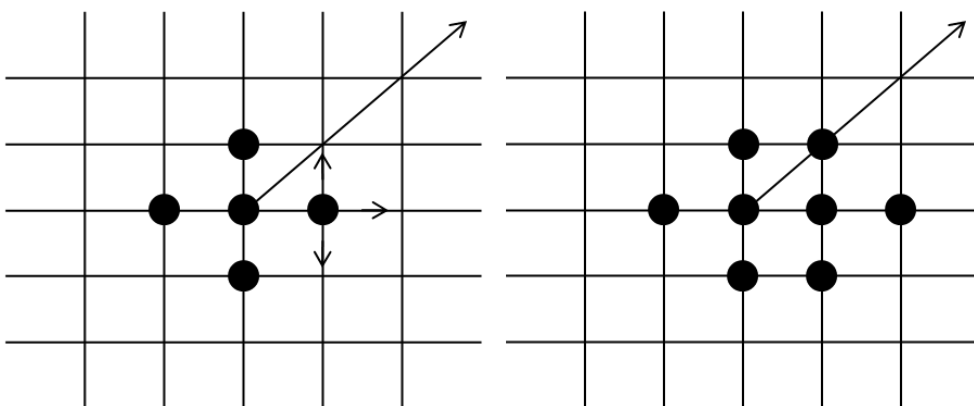


Figure 2-4. Initialization of the seed point and start of the fast marching method



[a] Calculating and updating new possible neighbors



[b] Selecting smallest possible value and again updating new possible neighbors

Figure 2-5. Updating process of the fast marching method in 2D.

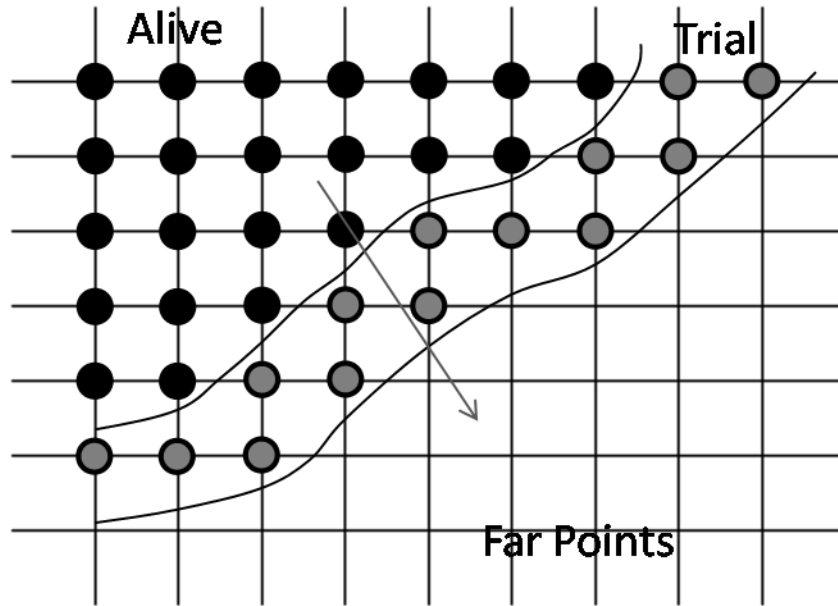


Figure 2-6. Overview of propagation of fast marching across a 2D grid.

(Figure 2-3- Figure 2-6 are reproduced from[24]) To compute a new time stamp at $U_{i,j,k}$, the following quadratic eikonal Equation 2.3 (discretized form of eikonal Equation 2.2 presented by Lorenz *et al.*[14]) is to be solved,

$$\left[\begin{array}{l} \max(D^x U_{i,j,k}, 0)^2 \\ + \max(D^y U_{i,j,k}, 0)^2 \\ + \max(D^z U_{i,j,k}, 0)^2 \end{array} \right] = (v_{i,j,k})^{-2} \dots \dots \dots (2.3)$$

Where:

$$D^x U_{i,j,k} = (U_{i,j,k} - U^x_{i,j,k}) / \Delta x \text{ where } U^x_{i,j,k} = \min(U_{i-1,j,k} - U_{i+1,j,k})$$

$$D^y U_{i,j,k} = (U_{i,j,k} - U^y_{i,j,k}) / \Delta y \text{ where } U^y_{i,j,k} = \min(U_{i,j-1,k} - U_{i,j+1,k})$$

$$D^z U_{i,j,k} = (U_{i,j,k} - U^z_{i,j,k}) / \Delta z \text{ where } U^z_{i,j,k} = \min(U_{i,j,k-1} - U_{i,j,k+1})$$

$\Delta x, \Delta y, \Delta z$ are the sampling distance between one voxel to the next voxel on the grid. Here the sampling distance is unity.

Assuming that $U^x_{i,j,k} \leq U^y_{i,j,k} \leq U^z_{i,j,k}$, three cases are distinguished:

1) The solution of the quadratic equation

$(D^x U_{i,j,k})^2 + (D^y U_{i,j,k})^2 + (D^z U_{i,j,k})^2 = (v_{i,j,k})^{-2}$ has to be real positive and larger than its neighbor voxels to be accepted as $U_{i,j,k}$, as we can see only at most three neighbor voxel can contribute to the value of $U_{i,j,k}$. If this is not the case

2) Then, $U_{i,j,k}$ has to be smaller than $U_{z,i,j,k}$, it means at most two neighbor voxel can contribute to the value of $U_{i,j,k}$ and the solution is given by equation

$(D^x U_{i,j,k})^2 + (D^y U_{i,j,k})^2 = (v_{i,j,k})^{-2}$. The solution has to be real positive and larger than $U_{y,i,j,k}$ to be accepted as new $U_{i,j,k}$.

3) Else, $U_{i,j,k}$ given by equation $U_{i,j,k} = U_{i,j,k}^x + \Delta x \cdot v_{i,j,k}^{-1}$ will be greater than $U_{x,i,j,k}$ and it will be accepted as $U_{i,j,k}$.

CHAPTER 3 MATERIALS AND METHODS

3.1 Materials

3.1.1 Anthropomorphic Phantom Data Set

Thin-slice X-ray Computed Tomography (CT) scans of an anthropomorphic lung phantom were used during development and preliminary testing of the vessel segmentation algorithm. These scans were downloaded from a publicly available database at the National Biomedical Imaging Archive (NBIA) [22]. The anthropomorphic thoracic phantom and the vasculature insert (Kyotokagaku Incorporated, Tokyo, Japan) were manufactured using urethane and epoxy resins to mimic the anatomy and CT-density of soft-tissue and bone respectively. Photographs of the exterior shell of the thoracic phantom and the vasculature insert are presented in Figure 3-1. A representative CT image is shown in Figure 3-2

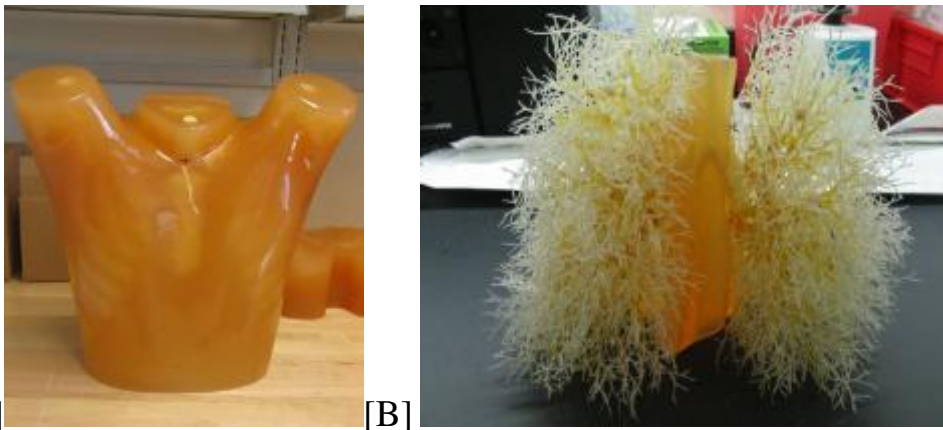


Figure 3-1. Exterior Shell of the Thoracic Platform and the Vasculature Phantom. [A] The picture on the left shows the exterior shell of the anthropomorphic thoracic phantom. [B] The picture on the right shows the vasculature phantom that was inserted in the shell.

CT data sets of the anthropomorphic phantom were used in the design and validation procedures of the algorithm. The data set used for developing the algorithm consisted of 198 CT slices of 2D Digital Imaging and Communications in Medicine

(DICOM) images acquired over the entire volume of the lung in the axial orientation. The images had a slice thickness of 3mm, inter-slice spacing of 1.5mm, and in-plane resolution of 512x512 pixels (0.78 mm x 0.78 mm). This data set was chosen because of its similarity in resolution to typical, diagnostic patient CT scans. The phantom was scanned using a Philips 16-row scanner (Mx8000 IDT, Philips Healthcare, MA).

3.1.2 Micro-CT Rat Data Set

Micro-CT data sets were acquired in excised lungs from healthy rats and rats with Pneum /MCT-induced pulmonary arterial hypertension. All animal work was performed by our colleagues at the University of Rochester, under the direction of Dr. R. James White. The procedures for animal handling were approved by the local Institutional Animal Care and Use Committee (IACUC) and in accordance with 'The Guide for the care and use of laboratory animals'. Male Sprague-Dawley (SD) rats, weights ranging from 200 - 250 grams, were induced with PAH by first removing the left hemi-lung (pneumonectomy), followed one week later by injection of 60 mg/kg monocrotaline (MCT)[3]. Rats with Pneum/MCT develop the key vascular features of human PAH. Normal (control) rats and rats with induced PAH were sacrificed at day 21. The rat lungs were then excised and the entire right middle lobe was imaged under micro-CT following perfusion of 30% barium sulfate contrast agent [25]. Briefly, the aorta was transected and the lung flushed with heparinized phosphate buffered saline and a nitric oxide donor to promote vasodilation. Thirty percent barium sulfate (v/v) in a 1% solution of low melting point agarose was injected in the RV outflow tract. The lung was then inflated with 10% formaldehyde at 15cm H₂O before using a micro-CT imaging system (Skyscan 1174) to scan at an isotropic resolution of 12 μ m. The reconstruction algorithm

was applied to planar images to obtain an isotropic reconstructed volumetric data set, 1304 × 1034 × 2000 voxels in dimension.

The data set used for developing the algorithm consisted of 500 micro-CT slices resized by 50% over the entire volume of the lung using routines built-in to MATLAB [26] and the NIH ImageJ [27] (<http://imagej.nih.gov/ij/>) programs. The resized images voxels were isotropic, with an inter-slice spacing of 0.048 mm, and in-plane resolution of 324x324 pixels (0.048 mm x 0.048mm). The algorithm was later tested on a larger data set with 2000 images that had an inter-slice spacing of 0.012mm and the same in-plane resolution (0.012mm x 0.012mm). In both cases, the phantom was scanned using a Skyscan 1174. The computations performed in this project were carried out using MATLAB and an enhanced, in-house version of ImageJ built by Dr. O'Dell, and run on 64-bit Windows and Mac Operating Systems.

3.2 Methods

The implementation of the three aims discussed in Chapter 1 is presented in this section. The results of the implementation are described in Chapter 4.

3.2.1 Automated Segmentation of Pulmonary Vasculature in the Anthropomorphic Phantom

The first milestone towards achieving the project goals was to implement the region-growing algorithm to segment the pulmonary vasculature and the fast marching algorithm to extract the lung morphology on the anthropomorphic phantom lung CT data set. The implementation was carried out in the following steps:

- i) Initial processing of DICOM image files
- ii) Extraction of lung volume
- iii) Initialization of seed points and time stamp
- iv) Segmentation of lung volume
- v) Morphology extraction

3.2.1.1 Initial processing of DICOM/TIFF image files

Axial slices for the entire input lung volume together comprised a 3D image data set. The DICOM/TIFF slices were read into MATLAB using the built-in function `dicomread/imread` and processed as a 3D array of pixel intensities. The 3D array `Img{z}(x,y)` was stored in a `.mat` file to avoid re-reading input files for future use. The MATLAB function `dicomread(filename)/imread(filename)` reads image data from the DICOM/TIIF file specified by the string `filename` [28]. A representative slice read into MATLAB is shown in Figure 3-2. The phantom does not contain lung parenchyma that contribute to background noise. Hence, no pre-processing was required for noise removal before the images were segmented.



Figure3-2. Representative 2D,axial CT images showing a cross-sectional slice of the 3Dimage data set of the anthropomorphic chest phantom, obtained from the NIH National Biomedical Imaging Archive.

3.2.1.2 Extraction of lung volume

The next step was to create a mask for the lung wall and heart so that the region growing and fast marching algorithms could be implemented on just the vessels present

in the inner lung volume. In this project we used the same method of Wang *et al.* [21] for the extraction of lung volume described in (2.3.1.1).

3.2.1.3 Initialization of seed points

Having isolated the lung volume, the next step was to select either one seed pixel or multiple seed pixels from which the vessel region would grow. Multiple seed points are necessary when the vessel tree branches are disconnected in the CT-reconstructed 3D volume or have multiple separate main branches. As vessels originate at the heart and diverge into smaller branches from there, the lung volumes are inspected for suitable seed pixels close to the heart.

3.2.1.4 Initialization of timestamp

The travel time of the propagating wavefront is computed methodically by the Euclidean Distance formula assuming a plane/zero curvature wave for the initial wavefront emanating from each seed point. This assumption is needed to reduce the numerical error caused by the first order equation for wavefront propagation given by Sethian [24], whose fast-marching approach is used in this thesis work. The travel time of the points surrounding the seed point was stored in a matrix and was assigned from nearest to farthest location automatically when the algorithm initiates. The newly assigned points constitute the spherical wavefront.

3.2.1.5 Voxel selection and segmentation

Segmentation of the arterial tree was performed using the approach of Govindarajan *et al.* [20], described in (2.3.1.2).

3.2.1.6 Morphology extraction

The segmented vascular tree structure was labeled using the fast marching method, as was explained in detail in section 2.3.2., but with additional constraints and

modifications as described below. The distance from the initial seed location to each voxel was calculated using the discretized eikonal equation (Equation 2.3) under the assumptions that the grid-point locations (voxels) were isotropically distributed and the speed of wave propagation was 1 grid-spacing per unit time.

All of the trial voxels comprise the expanding 3D wavefront (Figure 2.6 provides an illustration of the trial points as a wavefront). The continuity of the wavefront was checked repeatedly throughout the segmentation procedure for discontinuities that indicate the location of bifurcations in the vascular tree. For the vessel diameters of interest and the resolution of the available CT data, the optimal spacing between continuity checks was found to be every 3 - 5 time steps (a larger number of steps may be required for higher resolution images). The connectedness of the wavefront was assessed by applying the region growing algorithm at random-selected points along the wavefront. Additional check points were considered until all points along the wavefront were tagged as checked. Each voxel was tagged with the branch number to which it belongs. At each bifurcation point, each sub-front was given a new, consecutively-numbered branch number and we also recorded the number of the parent branch. This information was used to derive the parent-child relation and tree formation.

The main advantage of defining the length traversed along the centerline is that it gives the true branch length even if the curvature of vessel is high. So, each branch was processed individually, which helped in identifying the number of voxels per branch, branch length, centerline and average branch diameter. The average diameter was estimated from the length and number of voxels per branch using the assumption that the branch is cylindrical.

As they are traversed further away from the heart, the vessels are expected to either remain at the same size or reduce in diameter. A sudden increase in the apparent diameter of the vessel indicated that the region growing segmentation had leaked out of the vasculature. The radius of the each vessel was monitored throughout the region-growing operation to identify when the segmentation had leaked out of the vasculature.

Criteria for identifying vessel branches: To establish that a branch candidate represented a true pulmonary tree branch, three criteria were evaluated. First, the ratio of the branch length to radius ratio must have been greater than one. Second, the volume of the branch must have been at least 20% of the volume of the parent branch. And last, the radius of the branch had to be smaller than that of the parent branch. Branch segments that follow these three criteria were numbered in increasing order, indicating the total number of branches segmented at that stage in the wavefront propagation.

Center line: The centerline of a branch was derived by using the coordinates of all the voxels along the 3D wavefront in that branch. To define the centerline exactly along a curving branch, the centerline point from each of the wavefronts was calculated. The total number of points defining the centerline in a branch was equal to the number of wavefronts propagating through that branch. Since we are checking each 3D expansion wavefront after 5 unit radii (5 wavefront); we needed to classify each voxel into the closest wavefront. Each wavefront was maintained separately throughout propagation to assist in this classification. On finding the mean of the coordinates of all the voxels that belongs to same front and same branch, the centerline points are then computed by Equation 3-1.

$$[x_i \ y_i \ z_i]_B = \left[\left(\sum_{j=1}^N \frac{X_j}{N} \right)_i , \left(\sum_{j=1}^N \frac{Y_j}{N} \right)_i , \left(\sum_{j=1}^N \frac{Z_j}{N} \right)_i \right] \dots \dots \dots (3.1)$$

N = Number of voxels in the ith wavefront of branch B
i = Wavefront number
B = Branch number
X,Y,Z = Coordinate of Center line

Vessel length measurements: The second order discretized eikonal equation was used to calculate the distance along the centerline of each vessel, which was equated to the true vessel length. The number of voxels in a particular branch yielded the branch volume.

Branch angle: The branch angles were computed by first computing the vectors defined by the points along each branch centerline and in the neighborhood of the bifurcation. The first 20% of centerline points were used for the child branch vectors, and the last 20% of centerline points were used for the parent branch. The vector dot product was used to define the angle between the parent branch and each child branch. The field of vector for each branch was identified by averaging of small vectors represented by two consecutive points on the centerline segment.

$$[\vec{x}_p \ \vec{y}_p \ \vec{z}_p]_B = \left[\sum_{n=c8}^{c10} \frac{X_{n+1} - X_n}{N - 1} , \sum_{n=c8}^{c10} \frac{Y_{n+1} - Y_n}{N - 1} , \sum_{n=c8}^{c10} \frac{Z_{n+1} - Z_n}{N - 1} \right] \dots \dots \dots (3.2)$$

$$[\vec{x}_c \ \vec{y}_c \ \vec{z}_c]_{B+1} = \left[\sum_{n=c0}^{c2} \frac{X_{n+1} - X_n}{N - 1} , \sum_{n=c0}^{c2} \frac{Y_{n+1} - Y_n}{N - 1} , \sum_{n=c0}^{c2} \frac{Z_{n+1} - Z_n}{N - 1} \right] \dots \dots \dots (3.3)$$

$$\theta = \cos^{-1} \left[\frac{V_p \cdot V_c}{|V_p| |V_c|} \right] \dots \dots \dots (3.4)$$

: $[\vec{x}_p \vec{y}_p \vec{z}_p]_B$ And $[\vec{x}_c \vec{y}_c \vec{z}_c]_{B+1}$ = Vector for parent branch B (Vp) and child branch B+1 (Vc) respectively. B+1 indicates a child branch of B.

$[X_n Y_n Z_n]$ = nth voxel of branch B

c8 and c2 are centerline voxels where length is equal to 80% and 20% of total length of branch B respectively, C0 and c10 are start and end voxel of length.

N = Total number of voxel from c8 to c10 or from c0 to c2

Theta is the angle between parent and child branch.

It was difficult to define a branch angle between every child branch derived from single parent as we have found up to 5 children branch for a parent. So, we have calculated the bifurcation angle between parent branch and child branch not between child branches.

Tortuosity: The tortuosity of each branch was computed as the ratio of the true vessel length (along the centerline) to the minimum Euclidean distance between the two branch end points.

$$T_B = \left[\frac{L_B}{\sqrt{(X_1^c - X_{end}^c)^2 + (Y_1^c - Y_{end}^c)^2 + (Z_1^c - Z_{end}^c)^2}} \right] \dots \dots \dots (3.5)$$

Fractal dimension (FD) value: The FD value was calculated using the box count method applied to projection images of the segmented vascular volume. First, a mean-intensity projection of the 3Dsegmented vessel data set was generated along the x-axis, onto the 2Dy-z plane. Uniform 2D grids were generated over the projection plane where the size of each grid element – the box – was defined as an integer multiple of the original 2D in-plane pixel size. The smallest box size (corresponding to the most refined grid) was equal to the pixel size, and the largest box size (most coarse grid) corresponded to the entire projection plane. For a given box size, B_s (given in units of pixels), the software computed the number of boxes, N_b , that contained any part of a

vessel branch. Haitao *et al.* [29] presented a method to compute the FD value as the slope of $\log(N_b)$ versus $\log(B_s)$. Analogously, the FD value was computed for projection images also along each of the y and z- axes.

$$\text{Log}(N_b) = -\text{FD} * \text{Log}(B_s) + \text{Log}(K) \dots \dots \dots (3.6)$$

The mean of the resulting three FD values was used as the reported FD value. The reason for considering all three directions was to make the reported FD value more independent of the lung orientation in the imaging volume. A key characteristic of FD analysis is that the outcome is nearly independent of the original image resolution since the FD value is determined by the slope across a range of box sizes.

Normalized lung (NL) area: First, the mean intensity projection of the segmented 3D data sets along the x, y and z-axes were determined as described above. Then, the NL area was calculated as the ratio of the number of pixels on the image plane having gray-scale intensity value higher than zero over the total number of pixels on the image plane.

3.2.2 Outline of the Fast-Marching Algorithm

Initialization: First, tag seed voxel at zero distance and make it Alive. Then tag all 6 adjacent as Trial. Finally, tag all other remaining voxel as Far points. Initialize initial wavefront travel time to avoid larger error.

1. *Begin Loop: Set all points from the neighborhood of the seed point as Trial which satisfy threshold criteria, except the seed point which is already Alive.*
2. *Calculate the travel time at each trial point set above, using the quadratic equation.*
3. *Check: If wavefront travelled 5 unit radii*
 - a. *Check for disconnected in the wavefront*
Check if new segment satisfies criteria, if yes define the segment parameters.
4. *Classify each voxes into corresponding branch and front.*
5. *Calculate centerline points, parent to child relationships.*
6. *Select as the seed voxel for the next iteration the one with the smallest value of travel time among the Trial voxels.*
7. *Set the Trial voxel selected above as Alive; remove it from Trial group.*

8. *Return to top of loop*
9. *End, if no trial points are left.*
10. *Calculate metrics of morphology.*

3.3 Matlab Function

The extraction of the lung volume from the CT images was done by using the MATLAB function “bloodVesselSegmentation_Patient” made by Govindarajan *et al.*

The lung volume obtained from the above function was given to the MATLAB function srg3D made by Govindarajan *et al.* for segmentation of the arterial tree.

The segmented output obtained from the above function was given to the MATLAB function lunganalysis_3D for obtaining morphology of lungs.

lunganalysis_3D(img,seedPoint): This function was created to accept the segmented images as a 3D cell (img{i}(:)). The starting seed location was given as a point vector (x,y,z) and multiple seed points could be given as a row matrix. The output of this function gives the following list of parameters and indices: Number_branches_20, Number_of_Generation, Tortuosity, U (time stamp), branch, branchSorting, branch_angle, centreLine, radius, seedCount, slope_FDvalue and tree.

3.4 Validation and Analysis for the Automated Tool

The typical procedure to evaluate the performance of software tools for medical imaging applications is to compare the results to a known ground-truth. However, there is no definitive ground-truth available for verifying the extracted morphometry and associated metrics obtained for the pulmonary vasculature data sets obtained from rats or the anthropomorphic phantom. Thus, synthetic image data sets were generated. The ground truth for these was either known from the parameters used to generate the synthetic data sets or from manual evaluation of the data sets by an independent

reader. The outcomes from the ground-truth and the semi-automated software tool are provided in Table 3.2.

3.4.1 Validation Data Sets

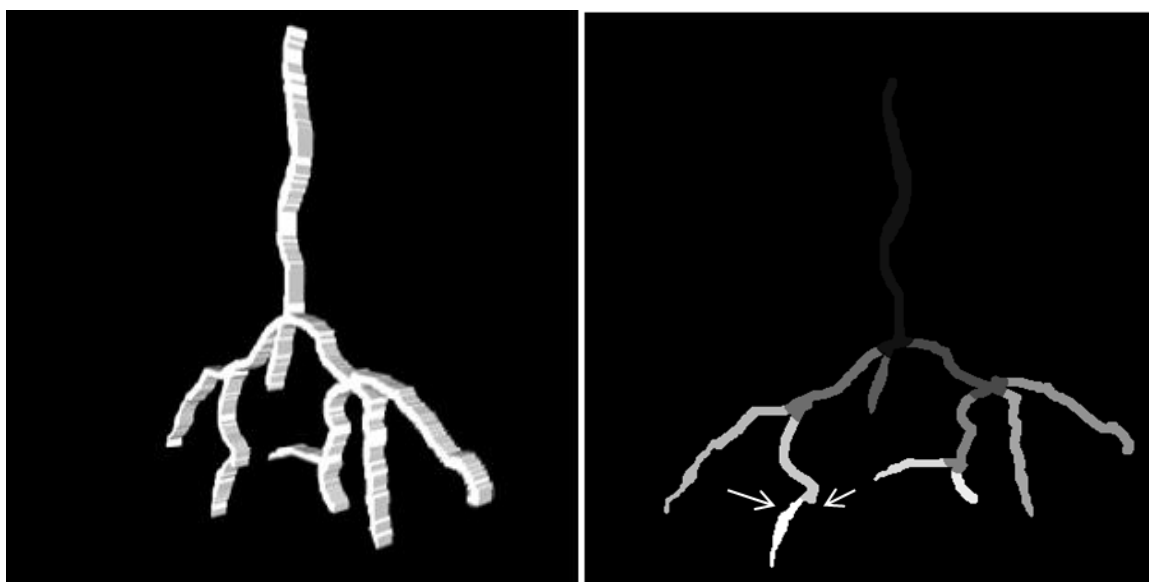
Seven synthetic data sets were generated to validate the software tools. The first three data sets (labeled #1-3) consisted of depictions of vessel trees of increasing complexity projected onto a 2D plane, and then extruded slightly into the third dimension to enable processing directly by the 3D analysis package. The ground truth was determined through manual assessment by an independent reader who was blinded to the results obtained from software tool. For these three synthetic data sets the reader was asked to determine the number of branch generations (number of generation shows the maximum number of branch derived from main branch in which seed point was placed) and number of branches. This was accomplished using the program Paint in Windows 7. In the first data set (labeled #1) the reader was asked also to compute the apparent radius for each branch.

The purpose for creating synthetic data sets #4-6 was to verify the parameters which cannot be obtained by the reader accurately, such as branch length, branch radius, branch angle and branch tortuosity. These three synthetic data sets (labeled #4-6) were generated from parametric models of cuboids and U-shaped structures where the length, radius, tortuosity and branch angle were known beforehand and used to generate the models. The ground truth for these data sets was compared with the results obtained from the tool and are provided in Table 3.2. The radius in the Table 3.2 for models was defined as the half-width of the cuboids and the length was defined as the height of each cuboid.

The last synthetic data set, labeled #7, was created from a subset of an actual rat micro-CT 3D lung volume wherein the 3D extent of each vessel was governed by that of the actual rat lung, in contrast to synthetic data sets 1-6 where an extrusion of a 2D image was performed. This data set was obtained by setting a higher grayscale threshold in the initial vessel segmentation step to reconstruct only the larger branches, thereby making the vasculature morphology simpler for the reader to process. The reader was asked to count the number of blood vessels using a plugin called 3D viewer in Image-J tool.

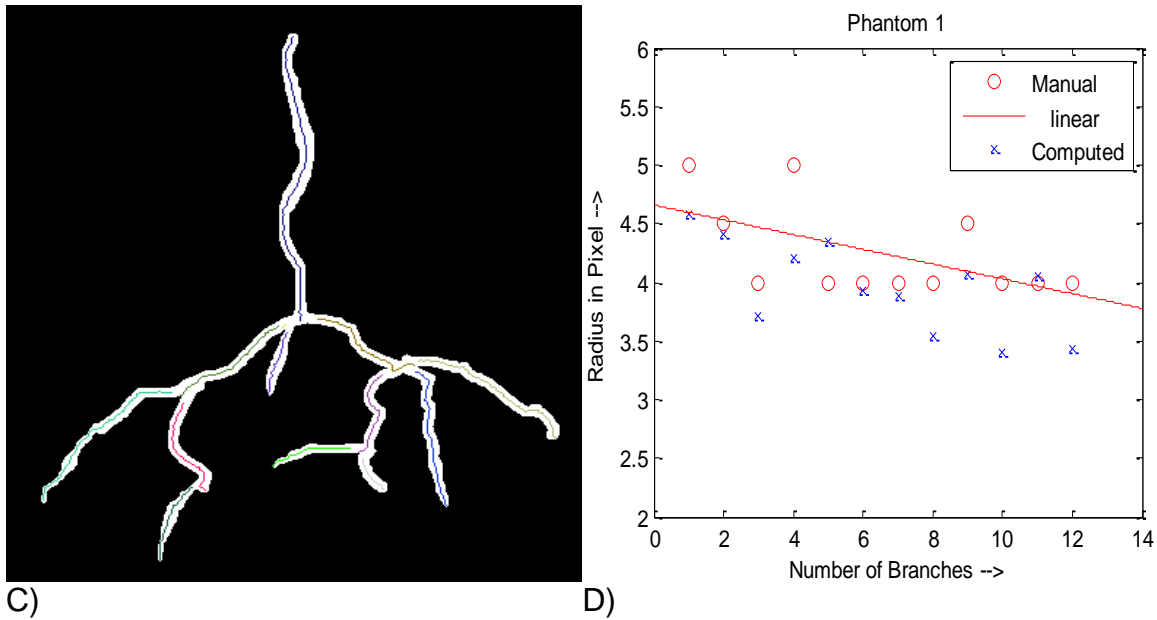
Synthetic Data Set 1

The number of branches calculated for the first synthetic data set by the tool was 12 and by the reader were 11. The difference was in a branch where one child was only a few pixels long (indicated by the white arrows in figure 3.3 [B]. The short child branch was did not satisfy the acceptance criteria for identifying vessel branches as described in section 3.2.1.6. The matching of the radii obtained for the phantom-1 was not perfect because the reader estimated the radius at one (2, 3) discrete location(s) while the



A)

B)



C) D)
 Figure 3-3. The first synthetic data set (#1) used to test the semi-automated vessel tree extraction software. The upper left image, [A], shows the 3D volume of the data set. [B] The upper right image is the output of the extraction tool, where each branch is given a unique gray-scale intensity. The white arrows show where a particular branch (described further in the text) is bifurcating. [C] The lower left image shows the branch centerlines obtained by the extraction tool, superposed in the image on top of the 2D projection of the synthetic data set. [D] The lower right graph compares the radius calculated manually that of my extraction tool.

algorithm estimated the average vessel radius (radius obtained shown in Table 3.1). In addition, the automatic tool computed the radii under the assumption that the vessel geometry was cylindrical while the actual phantom vessel was a cuboid (square in cross-section). The number of generations obtained from both methods was 4.

Table 3-1. Shows the radius obtained by the independent reader computed manually and obtained by my tool.

	Radius computed by tool	Radius Computed Manually
1)	4.37	5
2)	3.97	4
3)	4.40	4.5
4)	3.71	4
5)	4.21	5
6)	4.35	4
7)	3.93	4
8)	3.88	4
9)	3.54	4
10)	4.06	4.5
11)	3.40	4
12)	4.05	4
13)	3.43	4

Synthetic Data Set 2

The number of branches identified by the algorithm for the synthetic data set #2 was 94 while that for the human reader was 98. The number of generations obtained by the algorithm was 13 while the reader found 14. As with data set #1, the difference in branch number is due to the criteria for branch inclusion defined in 3.2.1.6 where a short child branch not 20% of the length of the parent branch was excluded. The centerline for each branch is computed individually therefore centerline is not connected from one branch to next branch.

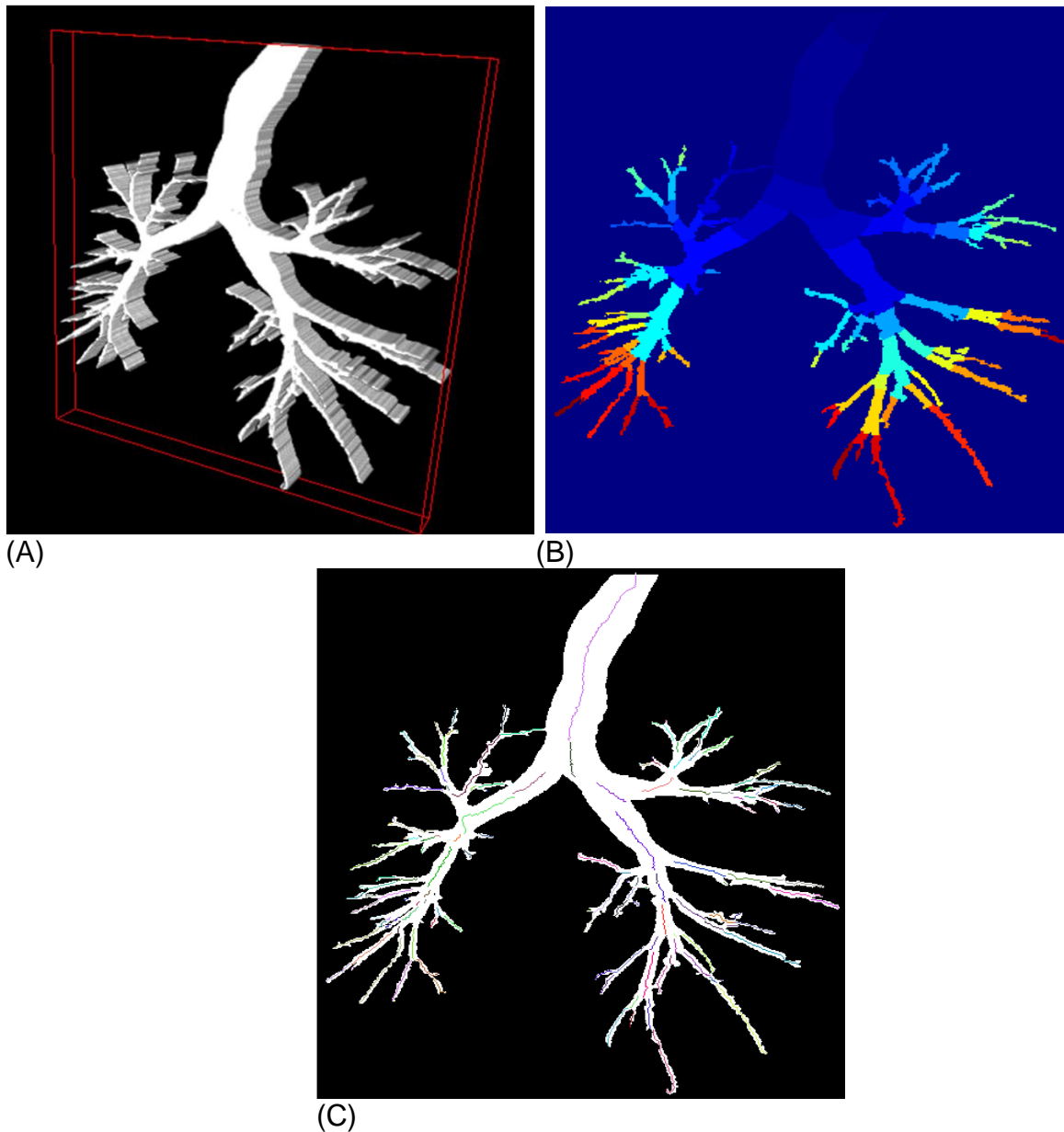
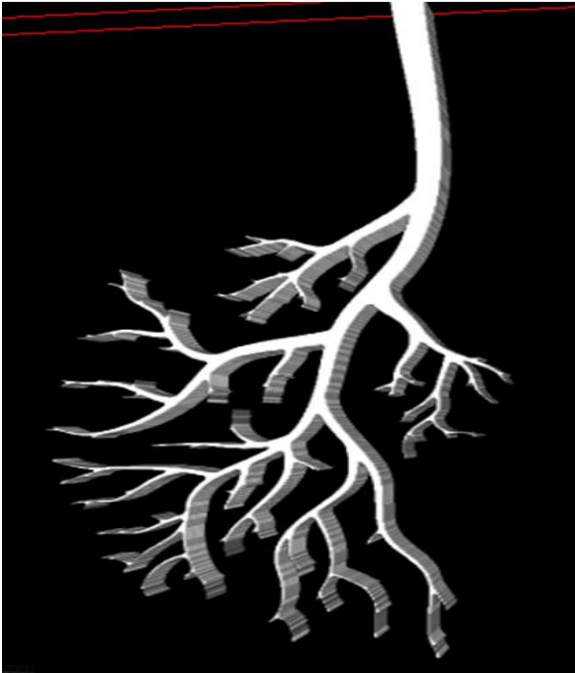
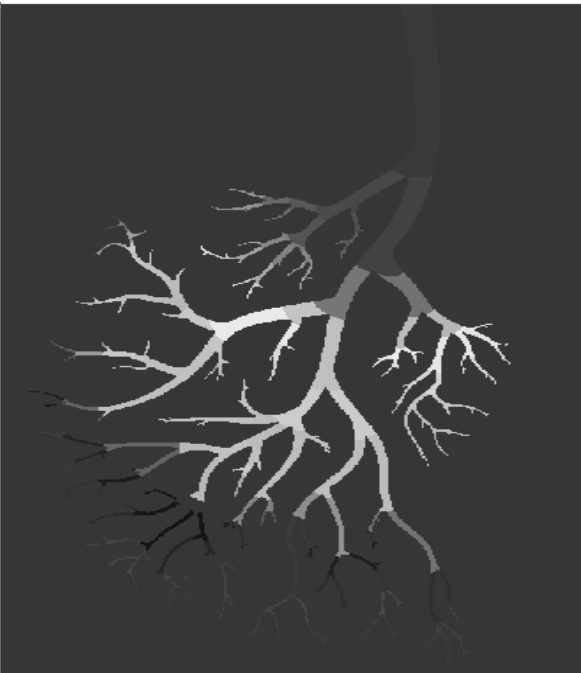


Figure 3-4. The second synthetic data set (#2) used to test the semi-automated vessel tree extraction software. The upper left image, [A], shows the 3D volume of the data set. [B] The upper right image shows the output of the extraction tool, where each branch is given a unique color. [C] The lower left image shows the branch centerlines obtained by the extraction tool, superposed in the image on top of the 2D projection of the synthetic data set.

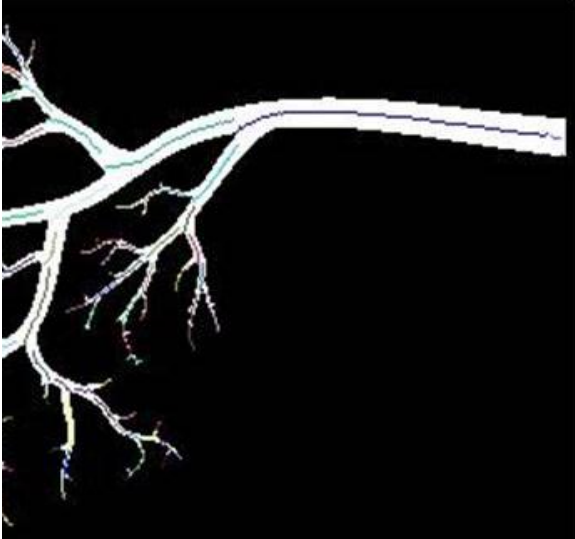
Synthetic Data Set 3



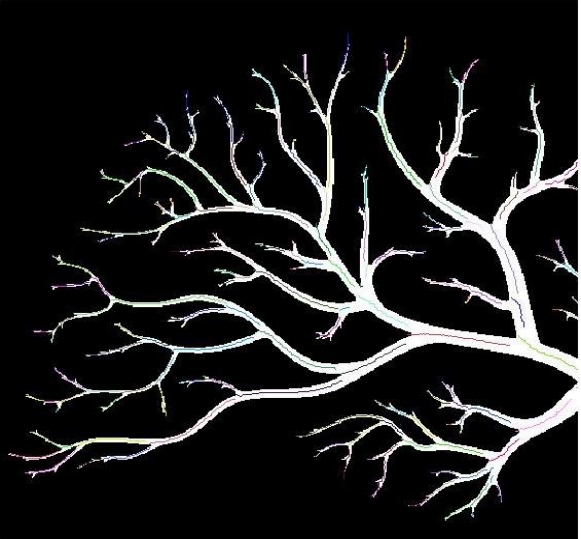
(A)



(B)



(C)



(D)



(E)

(F)

Figure 3-5. The third synthetic data set (#3) used to test the semi-automated vessel tree extraction software. The upper left image, [A], shows the 3D volume of the data set. [B] The upper right image shows a branch extracted by the tool, where each generation is shown in a different color. [C-F] The lower four images show the centerlines obtained by the tool, at increasing magnification. The centerline obtained by the algorithm appears to be accurate for even the smaller branches (2-3 pixels in radius).

The number of branches calculated for phantom-3 by the algorithm was 197 and that found manually was 201. The number of generations obtained by the algorithm was 13 and that found manually was 14.

Synthetic Data Set 4

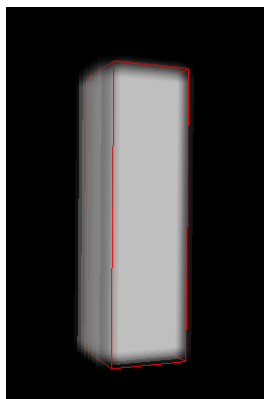


Figure 3-6. The fourth synthetic data set (#4) used to test the semi-automated vessel tree extraction software, cuboid model 3D image volume. The height of the cuboid was 50 pixels and the width/radius was 7 pixels.

Synthetic Data Set 5

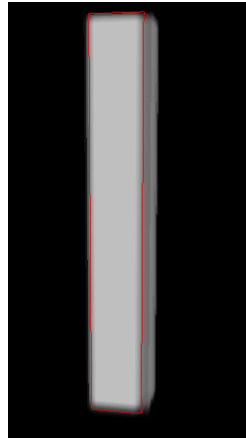


Figure 3-7. The fifth synthetic data set (#5) used to test the semi-automated vessel tree extraction software, cuboid model 3D image volume. The dimensions of the cuboid were 100*14*14 voxels. The height of the model was 100 pixels and width/radius was 7 pixels.

Synthetic Data Set 6

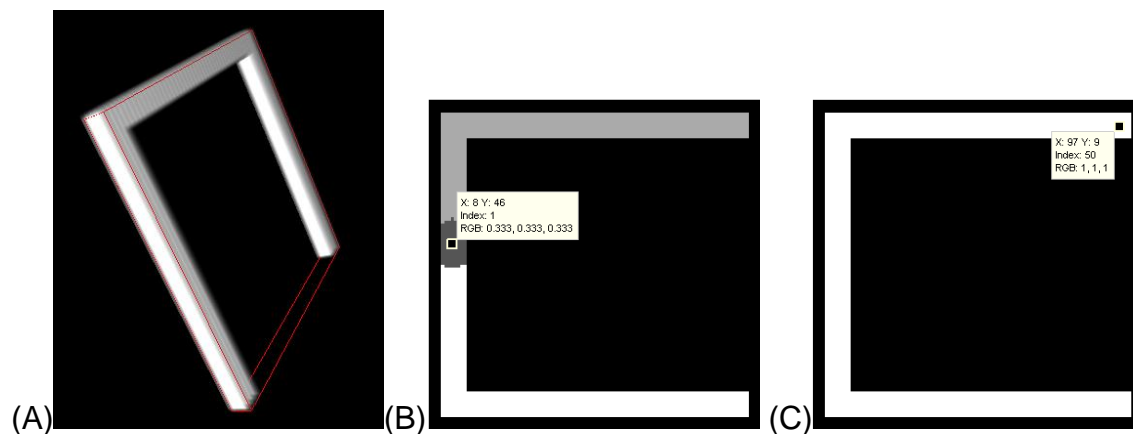


Figure 3-8. The sixth synthetic data set (#6) used to test the semi-automated vessel tree extraction software. [A] U-shaped model 3D image volume is shown in the left. The U-shape is made from three cuboids, each of dimension 100*16*16 voxels. [B] When the seed point was placed in the middle of the middle cuboid (as shown), the algorithm divided the U into three branches shown in different gray intensity. [C] When seed was placed at either of the two ends only one branch was obtained. The true length of the U-shape along centerline was 284 pixels and width was 16 pixels.

This U-shaped model was generated to test the algorithm's estimates of length, tortuosity, and branch angle. Two scenarios were tested, with a different seed point location for each. These are depicted in Figures 3.8 [B] and [C]. In the first scenario

where the seed was placed in center of the middle cuboid, the algorithm reconstructed three branches. This was because the initial branch divided into two branches as the wavefront divided into two after traveling some distance, as shown in Figure 3.8 [B]. The main idea to place the seed point in middle cuboid was to obtain these multiple branches, so that the tortuosity and the branch angle obtained through the tool could be tested. The angle between the seed point branch and two child branches was 0 degree and 180 degrees. The second scenario was to place at the end of the U-shape to test the algorithm's tortuosity calculation. Here, the vessel length was three times the end-point Euclidean distance. The true length of the U-shape along the centerline was 284 pixels and ends are separated by 92 pixels.

Synthetic Data Set 7

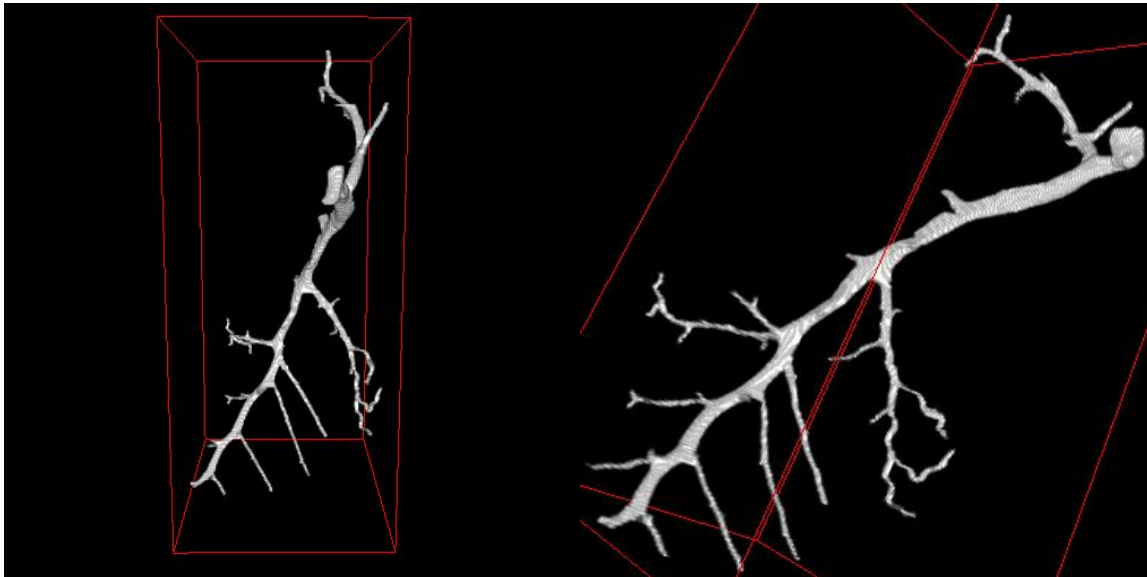


Figure 3-9. The seventh synthetic data set (#7) used to test the semi-automated vessel tree extraction software.

The last test data set was created from a subset of a real rat micro-CT lung data set. The reader manually counted 60 branches and 13 generations. The number of branches obtained by the algorithm was 54 and the number of generation was 13.

Table 3-2. Results compared with the ground truth obtained from the independent reader and results obtained from the tool. The length, radius, tortuosity results are shown for each branch individually.

	Metrics of vessel morphology	Computed by tool	Computed manually
1)	Number of Generations		
	Synthetic Data Set 1	4	4
	Synthetic Data Set 2	9	10
	Synthetic Data Set 3	13	14
	Synthetic Data Set 7	13	14
2)	Number of Branches		
	Synthetic Data Set 1	12	11
	Synthetic Data Set 2	94	98
	Synthetic Data Set 3	197	201
	Synthetic Data Set 7	54	60
3)	Length of branch (in pixels)		
	Synthetic Data Set 4	50.32	50
	Synthetic Data Set 5	99.2	100
	Synthetic Data Set 6	274.1	284
4)	Radius of branch(in pixels)		
	Synthetic Data Set 4	14.61	14
	Synthetic Data Set 5	14.42	14
	Synthetic Data Set 6	8.46	8
	Synthetic Data Set 1 (for 12 branches)		
5)	Branch Angle (in degree)		
	Synthetic Data Set 6 (seed point 1)	9	0
		171	180
6)	Tortuosity		
	Synthetic Data Set 4	1.01	1
	Synthetic Data Set 5	0.992	1
	Synthetic Data Set 6	2.98	3

3.4.2 Validation Results

The results obtained from the independent reader and from the tool are shown in Table 3.1 and Table 3.2, for each of the metrics, across each of the 7 synthetic data sets.

The number of generations and number of branches is correct within 10% error. The 10% error i.e. one generation was less or number of branches were less, when computed by tool as compared to manual computation is because we had considered only those branches as true branches which satisfy the criteria for branch explained in section 3.2.1.6. The length and radius outcomes match within 1% error and 5% error respectively. The tortuosity outcome within 1% error. Hence, the tool developed using region growing algorithm and fast marching algorithm can be successfully employed for morphological extraction of vasculature structure.

The results of the anthropomorphic phantom lung data set and rat data set as well as their performance analysis are presented in the following chapter.

CHAPTER 4 RESULTS

Presented in this chapter are the results obtained from the phantom lung images and rat micro-CT images, along with the metrics of vessel morphology in normal rats and PAH diseased rat. The statistical measurement between different metrics of vessel morphology is performed to determine one of metric as marker of PAH progression.

4.1 Anthropomorphic Phantom Lung CT Segmentation and Morphology Extraction

The semi-automatic segmentation algorithm was implemented on the anthropomorphic phantom lung CT data set described in Section 3.2.1.

4.1.1 Extraction of Lung Volume

The 2D CT slices were read into MATLAB as a 3D cell. The lung volume was extracted as described in (2.3.1.1).

4.1.2 Initialization of Starting Seed Point

Vessels within the extracted lung volumes were segmented by manually placing a seed point on large lung vessels located near where they emanate from the heart. For the phantom lung data set with 198 slices, the voxel at $x=256$, $y=218$, $z=80$ was chosen as the seed location for the right lung, and the voxel at $x=247$, $y=317$, $z=80$, for the left lung. Figure 4.1 shows the slice upon which the seed voxels were defined, as indicated by the gray arrows.

The maximum permissible value for difference (δ) between average intensity of the growing region and grayscale intensity of a newly added voxel was chosen as 500 Hounsfield units (HU).

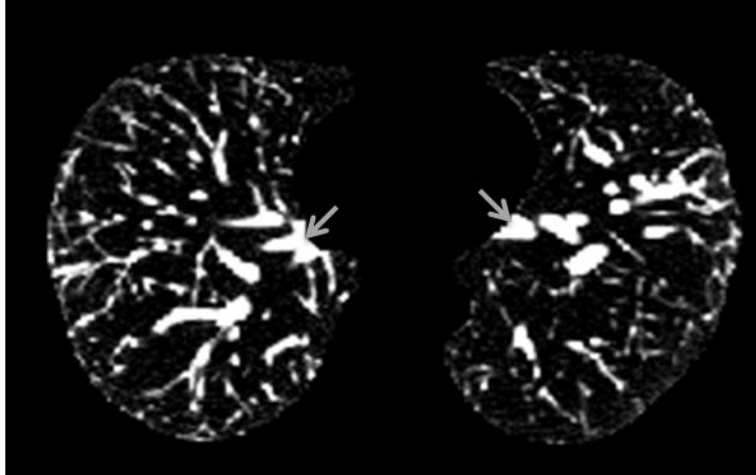


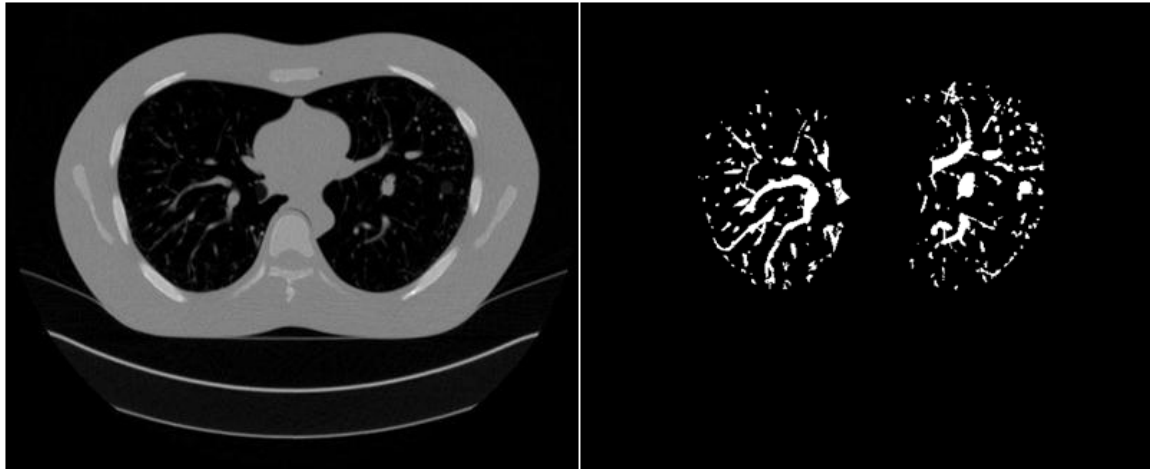
Figure 4-1. A CT image slice #80 in the anthropomorphic phantom showing seed point selection. Gray arrows show the position of the manually selected seed points in each hemi-lung.

4.1.3 Voxel Selection and Segmentation

The adaptive-threshold seeded region growing algorithm was performed using the MATLAB function `srg3D` on the lung volume. The maximum size of the region was set to 1,200,000 voxels. Starting from the initial seed, neighboring voxels were added to the vessel region until either the difference (δ) exceeded the predefined maximum or the number of voxels in the grown region exceeded 1200,000. The total time taken to segment the vascular tree from the phantom lung was 3 hours on a stand-alone Mac Pro workstation [Apple computers, Cupertino CA] running OS 10.6 with 1.2 GHz 12 core-processors and 12 Gig RAM, running MATLAB R2010b.

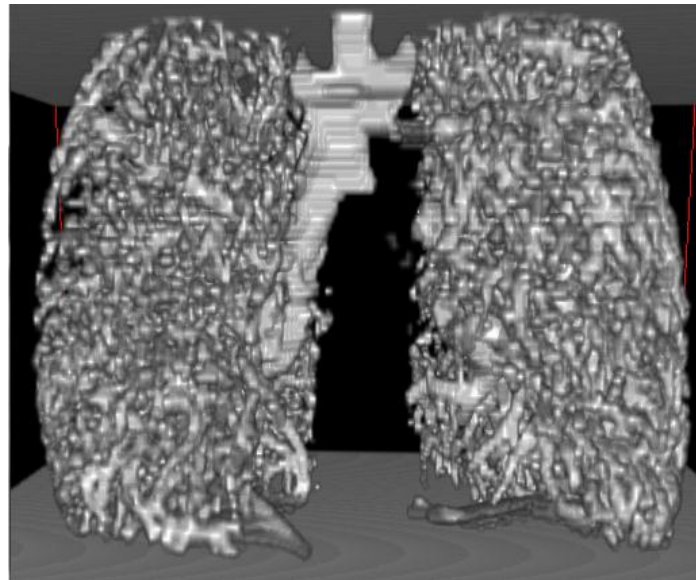
4.1.4 Morphology Extraction

The segmented vascular tree structure was used to extract the morphology using fast marching method by my MATLAB function `lunganalysis_3D`. The total time taken to extract the morphology of the lung was 30 minutes on a Windows7 Intel core i3 2.26 GHz processors running MATLAB R2010b.



[A]

[B]



[C]

Figure 4-2. Results of the vessel tree segmentation in the anthropomorphic phantom CT scanned at resolution of slice thickness 1.5mm and in-plane resolution 0.78 mm x 0.78 mm. Image [A] shows a representative 2D axial CT slice of the original image volume. Image [B] shows the segmented blood vessels corresponding to slice [A]. Image [C] shows the 3D rendering of the segmented vascular volume, viewed from the coronal plane, mid-way through the volume.

Intermediate results were recorded for every 200,000 voxels added to the vessel region. Figure 4-3 shows the 3D rendering of first six intermediate steps during the fast marching algorithm. The 3D rendering was achieved by using the Volume Viewer plugin in NIH ImageJ [27].

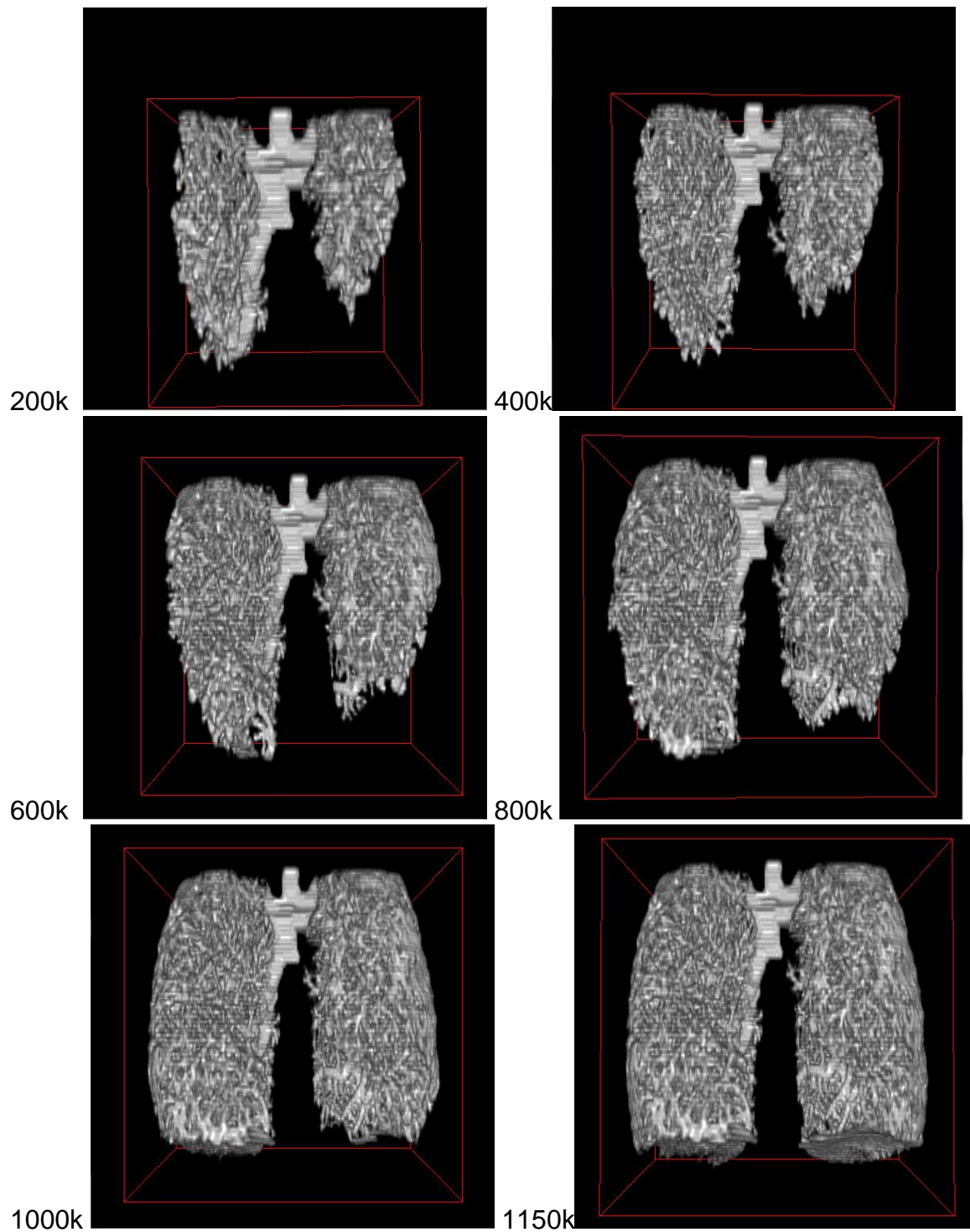


Figure 4-3. Rendering in 3D of the intermediate steps in the morphology extraction of the anthropomorphic phantom data set. The labels indicate the number of voxels contained in the vascular volume.

Table 4-1. Comparison between different metrics of vessel morphology to distinguish changes in vascular tree size when using different maximal voxel-count in the reconstruction of the vessels from the in CT anthropomorphic phantom data set.

Voxels Processed in (k)	Number of Branches	FD Value	Normalized Lung Area	Number of Generations	Correlation Coefficient between Branch Length and Branch Volume for p-value<0.05
50	48	-1.3711	0.0368	7	0.6404
100	155	-1.5053	0.0639	9	0.5771
200	334	-1.5800	0.1007	11	0.5770
300	710	-1.6483	0.1334	13	0.5627
400	1002	-1.6839	0.1635	14	0.5679
500	1462	-1.7180	0.1924	14	0.5527
600	1879	-1.7439	0.2197	14	0.5500
700	2275	-1.7663	0.2418	15	0.5552
800	2654	-1.7861	0.2614	16	0.5598
900	3011	-1.8055	0.2791	16	0.5602
1000	3695	-1.8222	0.2957	16	0.5597
1150	4244	-1.8413	0.3142	18	0.5511

Table 4-2. Correlation coefficient calculated between different metrics of vessel morphology in anthropomorphic phantom data sets.

Correlation coefficient for p-value (p<0.05)		
1)	Between FD Value and Normalized Lung Area	- 0.9670
2)	Between Number of Branches and Normalized Lung Area	0.9668
3)	Between Number of Branches and FD value	0.8838
4)	Between Voxels Processed and FD value	-0.9212
5)	Between Voxels Processed and Normalized Lung Area	- 0.9859

While extracting the morphology of the anthropomorphic lung data set, we stopped the algorithm at every 100k voxel (Figure 4.3 shows the 3D rendering of the intermediate steps). The basic idea behind stopping the algorithm at every 100k voxels is to mimic the progression of PAH in anthropomorphic data set, as in PAH patient the lungs vessel starts collapsing and losing lung vessel volume. The different volume of lungs from 1150k voxels to 50k voxels obtained at intermediate steps is assumed as PAH progression from normal lungs to severe PAH.

Table 4.1 shows comparison between different metrics of vessel morphology to distinguish changes in progression of PAH in anthropomorphic data set. The normalized lung area value lies between 0 and 0.6, where 0 is sever PAH and 0.6 is for normal lungs.

Table 4.2 shows the correlation coefficient between different metrics of vessel morphology in anthropomorphic phantom data sets. This correlation and the correlation obtained from real data set in section 4.2.3 was further used to define one of the metric as marker of PAH progression depend on which metric has shown strong correlation with most of the metrics of vessel morphology.

4.2 Micro-CT Rat Lung Segmentation and Morphology Extraction

The semi-automatic segmentation and morphology extraction algorithm was implemented on four normal/healthy and three PAH-diseased rat micro-CT data sets obtained from our collaborator, Dr. R. James White. A representative extracted vascular volume from a rat with PAH is shown in Figure 4-4. The metrics of vessel morphology measured are shown in Table 4-3.

The rat micro-CT data sets were obtained from excised lungs, so the preprocessing step of lung volume extraction (described in 3.2.1.2) was not required.

4.2.1 Initialization of Starting Seed Point

The pulmonary vascular trees were segmented by manually selecting a seed point in the large lung vessels, near the base toward where the heart would have been prior to excision. In some of the data sets the main vessels were found to be disconnected due to presence of an air bubble or possibly destruction of the vessel during the excision surgery. In most data sets, multiples main branches were seen. In each of

these cases, multiple seed points were necessary. Figure 4-4 shows an example of these cases.

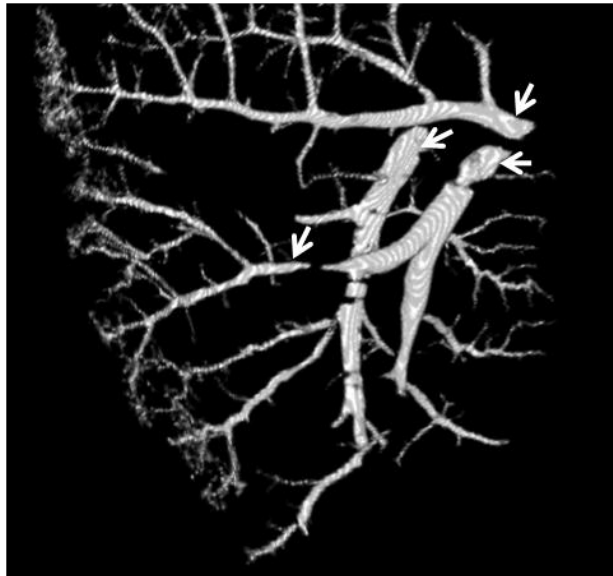
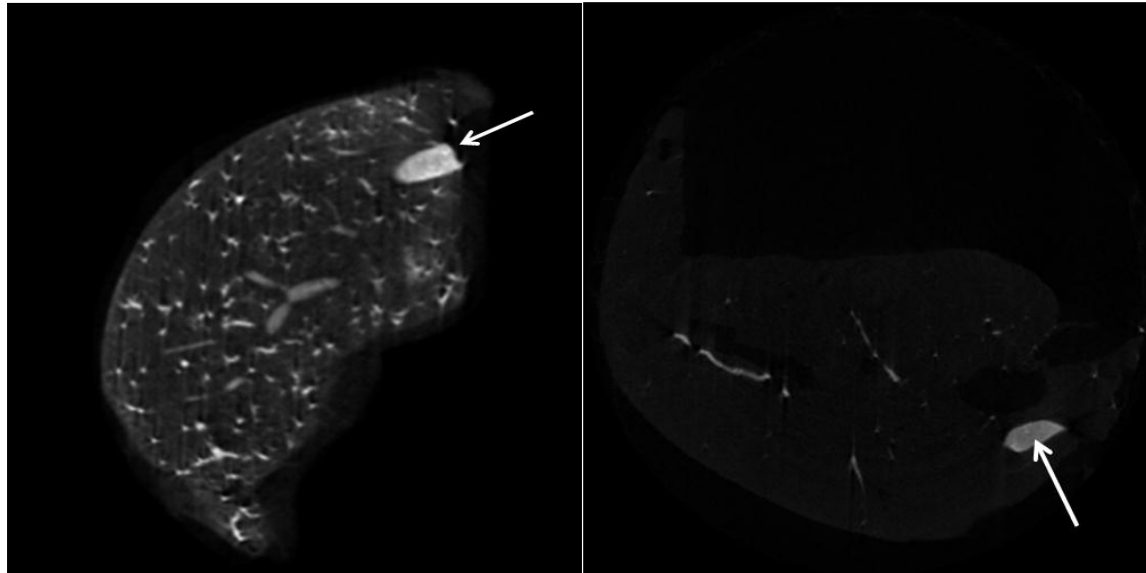


Figure 4-4. Shown are the multiple seed point selections (white arrows) in the 3D lung volume of a diseased rat lung data set exhibiting multiple main branches and branch discontinuities.

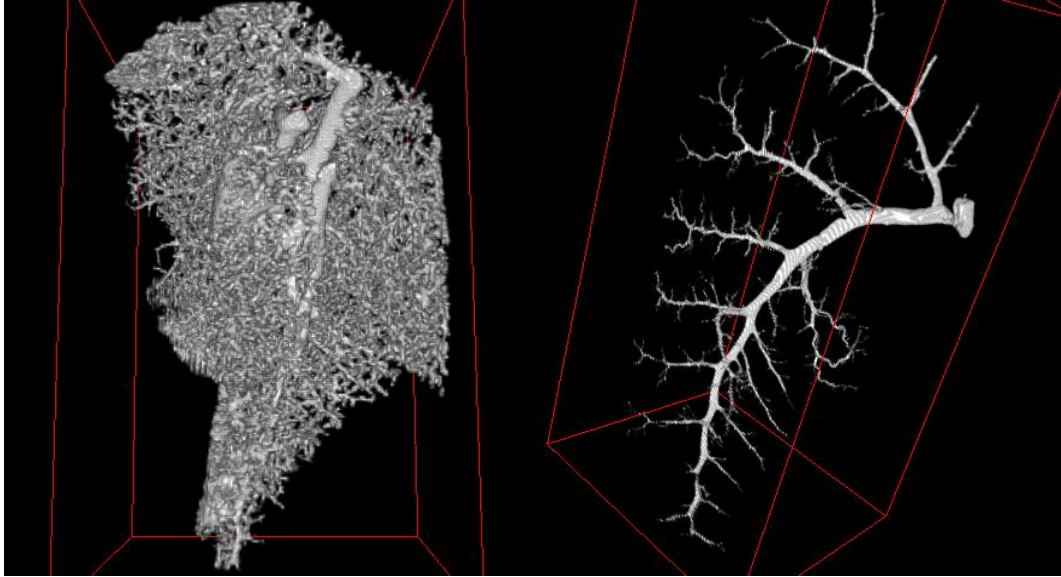


[A] [B]
Figure 4-5. Seed point selection in two different rat data sets. The image on the left, [A], shows a CT slice from healthy rat lung with the seed location indicated by the white arrow. The image on the right, [B], shows a slice through a diseased rat lung with the seed location indicated by the white arrow.

For each data set the maximum permissible value for difference (δ) between average intensity of the growing region and grayscale intensity of a newly added voxel was chosen as 500 Hounsfield units (HU).

4.2.2 Voxel Selection and Segmentation

The adaptive-threshold seeded region growing algorithm was performed to segment vasculature structure using the MATLAB function `srg3D` on the lung volume. The maximum size of the region was set to 1,200,000 voxels for an isotropic resolution 48 micron and for 12 micron resolution maximum size of the region can be set to 4,800,000 voxels. Starting from the initial seed, neighboring voxels were added to the vessel region until either the difference (δ) exceeded the predefined maximum or the number of voxels in the grown region exceeded 1,200,000. In an isotropic resolution of 48 micron the maximum number of voxels reached was 1,131,000. It is not always a good choice to increase the maximum size of the region to a very high value suppose if the algorithm leaks out of the blood vessel to outer tissue or fluid, than algorithm keep adding voxel to the vessel region because δ could not exceed the predefined maximum value and in such cases maximum size of the region 1,200,00 could be able to stop algorithm from growing. The total time taken to segment rat lung vessel was varied depending upon the number of voxels processed.



[A] [B]
 Figure 4-6. Results of the segmentation of rat lung vasculature. The image on the left, [A], shows a representative 3D volume of the healthy rat data set. The image on the right, [B], shows the 3D volume of the diseased rat data set.

4.2.3 Morphology Extraction

The extracted metrics of vascular morphology are listed in Table 4.3 and correlation coefficients among metrics of vessel morphology are listed in Table 4.4. For the plots shown in figure 4.7 through figure 4.10, each parameter were averaged and standard deviations were calculated over all of the healthy (n=4) and diseased (n=3) rat data sets. The parameters were plotted on a log scale on the Y axis. There are significant differences observed in the number of parameters in PAH diseased as compared to normal rats, including the number of branches, normalized lung area, FD value, vascular volume and correlation coefficient between branch length and volume.

The time to extract the morphology of the lung was 10-40 minutes on a Windows7 Intel core i3 2.26 GHz processors running on MATLAB R2010b. The time needed to extract the morphology depends on the number of voxels processed as there are large of voxels in healthy rats and smaller number of voxels in PAH diseased rats.

The Y-axis is shown on log scale. Figure 4.7 shows that a large number of the smaller and medium size vessels ranging from 50-100 microns are affected in PAH disease in rats as compared to 150-250 micron vessels. Figure 4.8 shows that a larger number of vessel ranging from 100-1000 microns length vessel are affected in PAH.

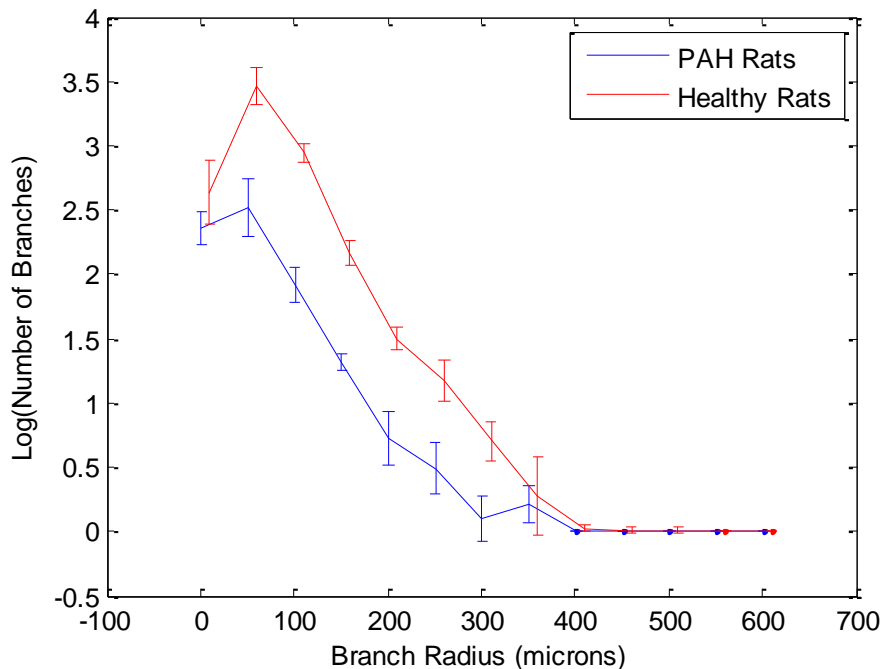


Figure 4-7. Histogram of radius of branch on log scale with standard deviation. Red color shows normal rat and blue color shows PAH diseased rat.

In Figure 4.7, each point represents the mean number of branches in 50 um of bin size (0-50um, 50-100um and so on) across 4 normal (red curve) and 3 PAH rats (blue curve), and the bars over every point represents the standard deviation. The X-axis represents the range of branch radii divided into bins. The X-axis is shown with a negative starting point for visual clarity of the first points.

In Figure 4.8, each point represents the mean number of branches in 500 um of bin size (0-500um length, 500-1000um length and so on) across 4 normal (red curve) and 3 PAH rats (blue curve), and the bars over every point represents standard

deviation .The X-axis represents the range of branch lengths divided into bins. The X-axis is shown with a negative starting point for visual clarity of the first points.

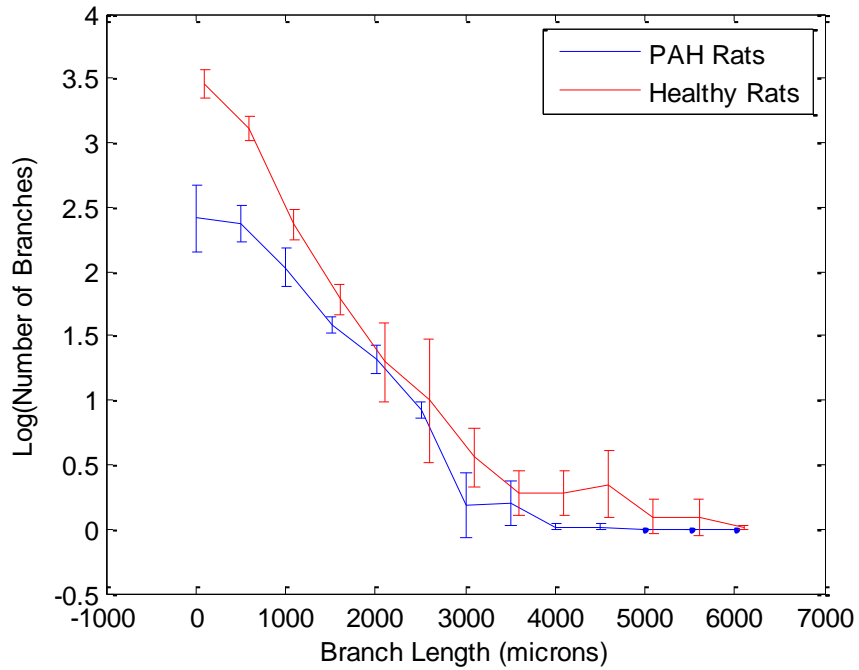


Figure 4-8. Histogram of length of branches on log scale with standard deviation. Red color shows normal rat and blue color shows PAH diseased rat.

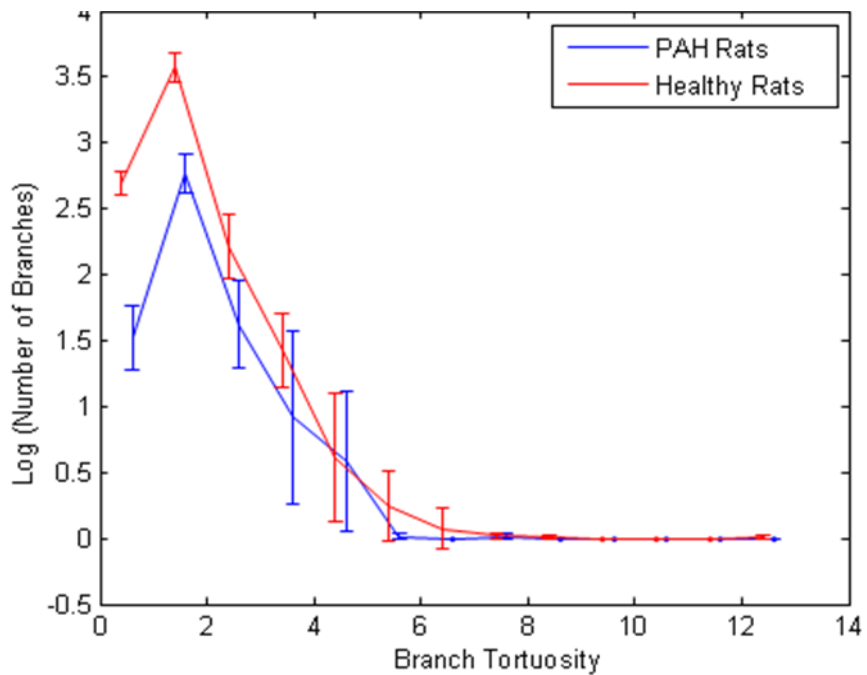


Figure 4-9. Histogram of branch tortuosity on log scale with standard deviation. Red color shows normal rat and blue color shows PAH diseased rat.

In Figure 4.9, each point represents the mean number of branches in bin size of 1 (0-1, 1-2 and so on) across 4 normal (red curve) and 3 PAH rats (blue curve), and the bars over every point represents standard deviation . The X-axis represents the range of tortuosity divided into bins.

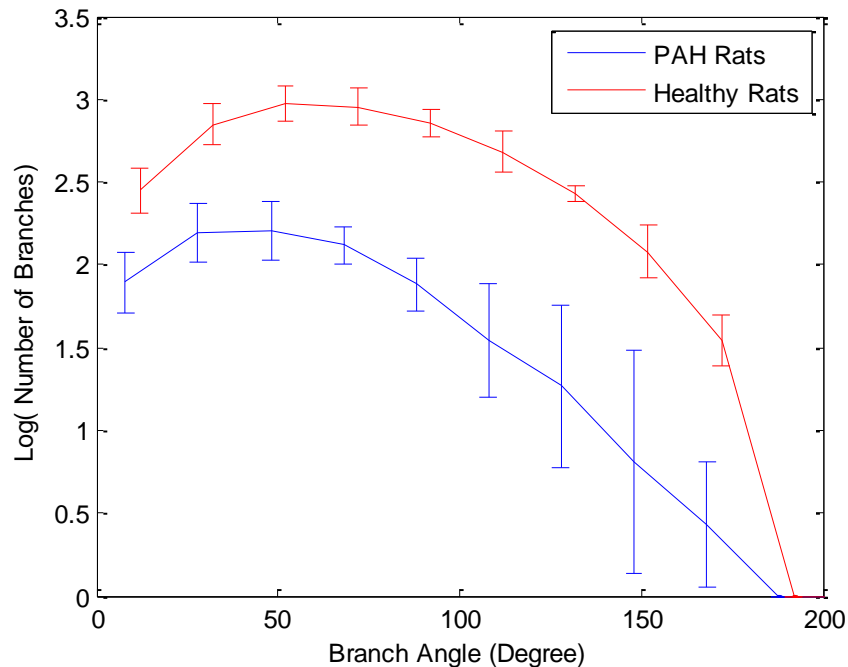


Figure 4-10. Histogram of branch angle on log scale with standard deviation. Red color shows normal rat and blue color shows PAH diseased rat.

In Figure 4.10, each point represents the mean number of branches in 20 degrees of bin size across 4 normal (red curve) and 3 PAH rats (blue curve), and the bars over every point represents standard deviation. The X-axis represents the range of branch length divided into bins.

In Figure 4.11, the ratio of branch length over branch radius is higher for PAH rat because in PAH there is pruning of smaller branches, which causes an increase in the mean length of the branch. In PAH rats, the radii of the branches decreases and the bar shifted to left hand side. Also, in PAH the vessel lumens of even the larger radius

branches are shrinking therefore there are no branches in the bin size of 401-500 microns.

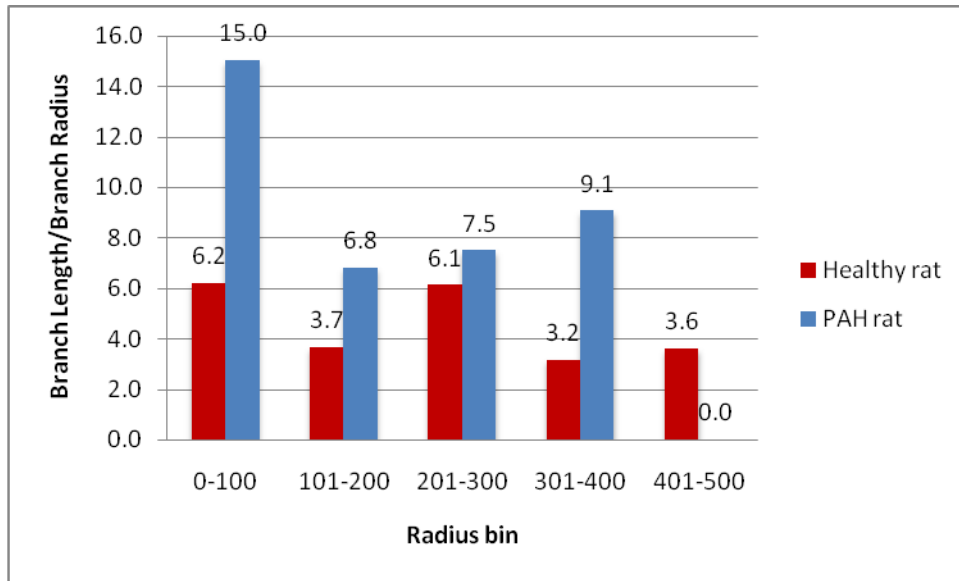


Figure 4-11. Histogram of the ratio of branch length over branch radius. Each bar in the figure represents the mean of the ratio of each branch in the bin size of 100 μm radius and the X-axis represents bins of different radius. Red color shows healthy rat and blue color shows PAH rat.

One data set had much less background image intensity and higher apparent contrast between the small vessels and the background signal. In this data set the threshold seeded region growing algorithm was able to detect a much larger number of smaller vessels, nearly twice as many, compared with the other 3 normal rat data sets.

Table 4.3. Comparison between different metrics of vessel morphology in healthy and PAH rat lungs scanned with micro-CT. Shown also is the correlation coefficient between each branch length and branch volume for p-value<0.05

Voxels Processed in (k)	Volume Cm ³	Number Of Branches	FD Value	Normalized Lung Area	Number of Generations	Correlation Coefficient
Healthy Data Sets						
1131	125.1	8179	-1.9235	0.4859	31	0.6116
730	80.7	4078	-2.0330	0.5292	26	0.6994
750	82.9	2362	-2.0609	0.5070	22	0.7155
950	105.1	3985	-2.0303	0.5397	34	0.6765
Diseased Data Sets						
144	15.9	583	-1.7606	0.1862	26	0.4582
125	13.8	451	-1.7121	0.1252	22	0.4737
150	16.6	728	-1.8252	0.1898	26	0.3796

Table 4-4. Correlation coefficient calculated between different metrics of vessel morphology in rat data sets.

Correlation coefficient for p-value (p<0.05)		
1)	Between FD Value and Normalized Lung Area	- 0.9558
2)	Between Number of Branches and Normalized Lung Area	0.7379
3)	Between Number of Branches and FD value	-0.5378
4)	Between Volume and FD value	-0.7972
5)	Between Volume and Normalized Lung Area	0.9296
6)	Between Volume and Number of branches	0.9108

The linear regression R-squared value for linear fit between normalized lung area (computed via multiple mean-intensity projections as described in section 3.2.1.6) and vascular volume is 0.9720. This R-squared values shows that the linear equation $0.00025 * x + 0.051$ predicts 97.2% of the variance in the normalized lung image area. It means there is a strong linear relationship between the vascular volume and the normalized lung area, and also the volume has good correlation with other metrics of vessel morphology for both rat and anthropomorphic data sets as shown in Table 4.4 and Table 4.2. Therefore, normalized lung area can be used as for a marker for PAH disease progression.

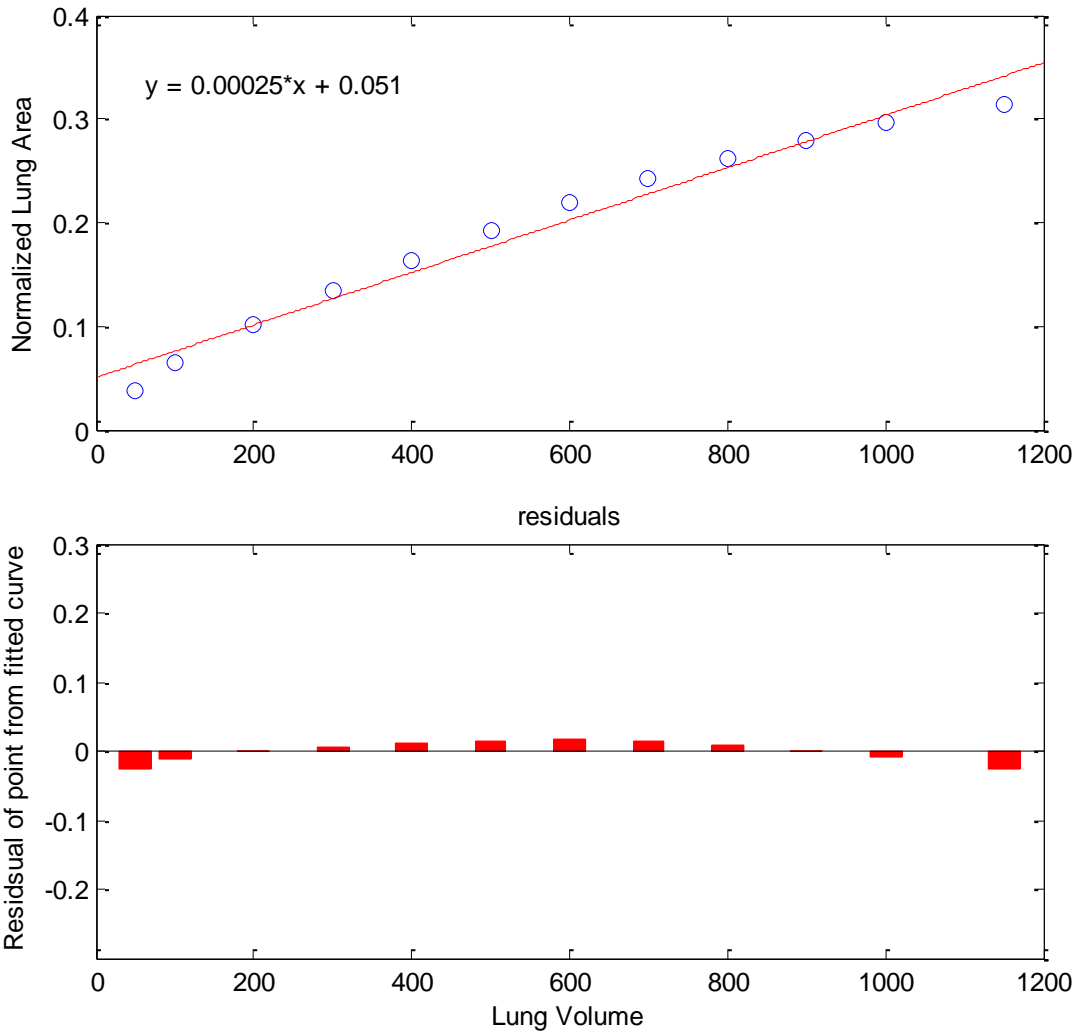


Figure 4-12. Linear fit between normalized lung area and total lung vascular volume. The residual plot shows the deviation of normalized lung area from the fitted curve.

CHAPTER 5 DISCUSSION

An image-based fast marching algorithm was developed, optimized and applied in synthetic and real lung CT image data sets to semi-automatically extract and characterize the morphology of pulmonary vasculature structure. For each vessel branch, the length, radius, angle, tortuosity, centerline, length to radius ratio, vascular volume and number of descending segments were determined. The approach was validated on a series of 7 different synthetic vascular tree image sets. In the micro-CT lung scans of 4 healthy rats, an average of 5,000 vessel branches were identified, while in rats with PAH an average of only 500 branches were identified. These results followed the expectations of our clinical colleagues and the trends apparent from visual inspection of the healthy and PAH rat lung data sets.

The relationship between the volume and length each branch, compiled over all extracted branches, was also examined and a difference was found between normal and PAH diseased rat data sets. The normalized lung area and fractile dimension (FD) value can be used as a marker of the extent of PAH. The variation in lung morphology from healthy to PAH rats is also detectable in length, branch angle, total vascular volume and tortuosity.

The processing took an average of 30 minutes per data set for image volumes of size $326 \times 326 \times 424$ voxels using a laptop PC with 2.26 GHz Intel core i3 processor, 4 GB RAM, compiled by MATLAB and using the Windows 7 Home premium operating system.

Explanation of the initialization parameters used in the current algorithm:

Although user input was not required during every implementation of the algorithm, some of the variables in the algorithm had to be optimized for different data sets. The variables and their significance are presented here in the same order they are called during the segmentation.

5.1 Time Stamp

Once a seed point is initialized, the travel time calculated at the surrounding isotropic, sparse grid-points can contain large errors up to 20% in the first wavefront emanating from the initial seed point. This occurs because of very high curvature of the spherical wavefront near the seed point. The error diminishes at locations far from the seed point, as described by Stanford *et al.* [30].

5.2 Wavefront Radius

Smaller wavefronts have higher sensitivity for detecting the smaller-length vessels, but if the wavefront radius is too small then the algorithm may erroneously identify one branch as two because it is hard to check the connectivity of a wavefront in large vessels due to the dome shape of each wavefront. There is tradeoff when trying to optimize between detecting very small and very large vessels. Another constraint is that for the same vessel radius a higher wavefront radius is needed for the higher resolution (higher number of voxels per unit radius) data set. For the rat data sets, the wavefront radius was taken as 5 voxels, meaning that five fronts together define one wavefront for my morphological analysis. For lower resolution (2 mm to 3 mm per voxel dimension) data sets, such as those used in most patient scans, wavefront radii as small as 3 mm can be used.

CHAPTER 6 CONCLUSION AND FUTURE WORK

6.1 Conclusion

The region-growing and the fast marching algorithms of Aim 1 were applied to thin-slice CT scans of anthropomorphic phantom lungs that present with no background noise. Successful isolation of the lung volumes, initial seed placement vessel segmentation and morphological extraction has all been demonstrated. In Aim 2, the tool was validated by the using the ground truth obtained from an independent reader and/or the model parameters used to generated the synthetic data sets. In Aim 3 multiple metrics to quantify/identify PAH disease in rats were computed and compared.

In conclusion, we have designed and developed an efficient semi-automatic tool that is able to quantify morphological changes in pulmonary vasculature due to PAH. The algorithm can identify blood vessels as small as 30-40 microns in radius in rats, where the minimum size is governed primarily by the resolution of the image.

The algorithm can be modified for use in other imaging modalities or clinical applications. This work has potential application in other diseases where there is loss of pulmonary vasculature, such as pulmonary emboli, emphysema and chronic bronchitis. There may also be application to other organs such as the colon and heart.

6.2 Limitations and Future Work

One of the limitations of this tool is the need for an isotropic grid for wavefront propagation. However it is theoretically possible to extend this work to anisotropic grids through the use of a Jacobian matrix to keep track of the different length scales in each direction.

In the future, this tool could be used for extraction of morphology of lungs in PAH-induced rats given also an agent thought to improve the repair response, such as Ixolaris [11]. Thus this tool may prove to be primarily important for assessment of the efficacy of emerging drugs and for detection of the extent of PAH.

A future improvement would be to optimize this tool for detection of the extent of pulmonary changes in PAH in humans using MRI and/or CT scans. I envision that the rate of disease progression could be assessed from CT scans acquired over period of time in the same patient and the changes quantified in the manner demonstrated in Table 4.1. Here the algorithm was stopped at progressively larger maximum voxel counts to mimic the changes that would be seen in a developing lung, but in PAH without intervention the patient's lung vascular volume will be expected to decrease over time.

REFERENCES

- [1] V. V. McLaughlin, S. L. Archer, D. B. Badesch, R. J. Barst, H. W. Farber, J. R. Lindner, M. A. Mathier, M. D. McGoon, M. H. Park, R. S. Rosenson, L. J. Rubin, V. F. Tapson, and J. Varga, "ACCF/AHA 2009 Expert Consensus Document on Pulmonary Hypertension: A Report of the American College of Cardiology Foundation Task Force on Expert Consensus Documents and the American Heart Association Developed in Collaboration With the American College of Chest Physicians; American Thoracic Society, Inc.; and the Pulmonary Hypertension Association," *Journal of the American College of Cardiology*, vol. 53, no. 17, pp. 1573–1619, Apr. 2009.
- [2] G. Simonneau, N. Galiè, L. J. Rubin, D. Langleben, W. Seeger, G. Domenighetti, S. Gibbs, D. Lebrec, R. Speich, M. Beghetti, S. Rich, and A. Fishman, "Clinical classification of pulmonary hypertension," *Journal of the American College of Cardiology*, vol. 43, no. 12, Supplement, p. S5–S12, Jun. 2004.
- [3] R. J. White, D. F. Meoli, R. F. Swarthout, D. Y. Kallop, I. I. Galaria, J. L. Harvey, C. M. Miller, B. C. Blaxall, C. M. Hall, R. A. Pierce, C. D. Cool, and M. B. Taubman, "Plexiform-like lesions and increased tissue factor expression in a rat model of severe pulmonary arterial hypertension," *American Journal of Physiology - Lung Cellular and Molecular Physiology*, vol. 293, no. 3, p. L583 – L590, 2007.
- [4] N. Rudarakanchana, R. C. Trembath, and N. W. Morrell, "New insights into the pathogenesis and treatment of primary pulmonary hypertension," *Thorax*, vol. 56, no. 11, pp. 888 –890, Nov. 2001.
- [5] N. F. Voelkel and R. M. Tuder, "Cellular and molecular mechanisms in the pathogenesis of severe pulmonary hypertension," *Eur. Respir. J.*, vol. 8, no. 12, pp. 2129–2138, Dec. 1995.
- [6] S. M. Kawut, E. M. Horn, K. K. Berekashvili, R. P. Garofano, R. L. Goldsmith, A. C. Widlitz, E. B. Rosenzweig, D. Kerstein, and R. J. Barst, "New predictors of outcome in idiopathic pulmonary arterial hypertension," *The American Journal of Cardiology*, vol. 95, no. 2, pp. 199–203, Jan. 2005.
- [7] K. L. Hassell, "Altered hemostasis in pulmonary hypertension," *Blood Coagul. Fibrinolysis*, vol. 9, no. 2, pp. 107–117, Mar. 1998.
- [8] J. K. Damås, K. Otterdal, A. Yndestad, H. Aass, N. O. Solum, S. S. Frøland, S. Simonsen, P. Aukrust, and A. K. Andreassen, "Soluble CD40 ligand in pulmonary arterial hypertension: possible pathogenic role of the interaction between platelets and endothelial cells," *Circulation*, vol. 110, no. 8, pp. 999–1005, Aug. 2004.

- [9] J. H. Newman, B. L. Fanburg, S. L. Archer, D. B. Badesch, R. J. Barst, J. G. N. Garcia, P. N. Kao, J. A. Knowles, J. E. Loyd, M. D. McGoon, J. H. Morse, W. C. Nichols, M. Rabinovitch, D. M. Rodman, T. Stevens, R. M. Tuder, N. F. Voelkel, and D. B. Gail, "Pulmonary arterial hypertension: future directions: report of a National Heart, Lung and Blood Institute/Office of Rare Diseases workshop," *Circulation*, vol. 109, no. 24, pp. 2947–2952, Jun. 2004.
- [10] H. W. Farber and J. Loscalzo, "Pulmonary arterial hypertension," *The New England journal of medicine*, vol. 351, no. 16, pp. 1655–1665.
- [11] R. J. White, R. F. Swarthout, and D. F. Meoli, "Ixolaris, a tissue factor inhibitor, reduces vascular pruning and delays death in rats with established pulmonary arterial hypertension. . 22 (1): 1209.4 - The FASEB Journal."
- [12] L. Zhou, M. S. Rzeszotarski, L. J. Singerman, and J. M. Chokreff, "The detection and quantification of retinopathy using digital angiograms," *IEEE Trans Med Imaging*, vol. 13, no. 4, pp. 619–626, 1994.
- [13] C. Pisupati, L. Wolff, and E. Zerhouni, "Segmentation Of 3D Pulmonary Trees Using Mathematical Morphology," *Proc. Mathematical Morphology and its Applications to Image and Signal Processing, Atlanta*, pp. 409–416, 1996.
- [14] C. Lorenz, S. Renisch, T. Schlathoelter, and T. Buelow, "Simultaneous segmentation and tree reconstruction of the coronary arteries in MSCT images," *Proceedings of SPIE*, vol. 5031, no. 1, pp. 167–177, May 2003.
- [15] N. Niki, Y. Kawata, and T. Kumazaki, "Three-dimensional image analysis of blood vessels using cone-beam CT," in *Nuclear Science Symposium and Medical Imaging Conference, 1994., 1994 IEEE Conference Record, 1994*, vol. 4, pp. 1519–1523 vol.4.
- [16] T. Wischgoll, J. S. Choy, and G. S. Kassab, "Extraction of morphometry and branching angles of porcine coronary arterial tree from CT images," *Am. J. Physiol. Heart Circ. Physiol.*, vol. 297, no. 5, pp. H1949–1955, Nov. 2009.
- [17] W. E. Higgins, W. J. . Spyra, and E. L. Ritman, "Automatic extraction of the arterial tree from 3-D angiograms," in *Engineering in Medicine and Biology Society, 1989. Images of the Twenty-First Century., Proceedings of the Annual International Conference of the IEEE Engineering in*, 1989, pp. 563–564 vol.2.
- [18] T. Tozaki, Y. Kawata, N. Niki, H. Ohmatsu, and N. Moriyama, "3-D visualization of blood vessels and tumor using thin slice CT images," in *Nuclear Science Symposium and Medical Imaging Conference, 1994., 1994 IEEE Conference Record, 1994*, vol. 3, pp. 1470–1474 vol.3.

- [19] A. Bush, C. M. Busst, S. G. Haworth, A. A. Hislop, W. B. Knight, B. Corrin, and E. A. Shinebourne, "Correlations of lung morphology, pulmonary vascular resistance, and outcome in children with congenital heart disease.," *Br Heart J*, vol. 59, no. 4, pp. 480–485, Apr. 1988.
- [20] S. T. Govindarajan, S. Chandrasekharan, and W. O'Dell, "Automated segmentation of blood vessels in the presence of fibrosis in volumetric lung CT images," 2011.
- [21] P. Wang, A. DeNunzio, P. Okunieff, and W. G. O'Dell, "Lung metastases detection in CT images using 3D template matching," *Medical Physics*, vol. 34, no. 3, p. 915, 2007.
- [22] M. A. Gavrielides, L. M. Kinnard, K. J. Myers, J. Peregoy, W. F. Pritchard, R. Zeng, J. Esparza, J. Karanian, and N. Petrick, "A resource for the assessment of lung nodule size estimation methods: database of thoracic CT scans of an anthropomorphic phantom," *Opt Express*, vol. 18, no. 14, pp. 15244–15255, Jul. 2010.
- [23] R. Adams and L. Bischof, "Seeded region growing," *IEEE Transactions on Pattern Analysis and Machine Intelligence*, vol. 16, no. 6, pp. 641–647, Jun. 1994.
- [24] J. A. Sethian, "Fast Marching Methods," *SIAM Review*, vol. 41, no. 2, pp. 199–235, Jun. 1999.
- [25] C. L. Duvall, W. R. Taylor, D. Weiss, and R. E. Guldberg, "Quantitative microcomputed tomography analysis of collateral vessel development after ischemic injury," *Am. J. Physiol. Heart Circ. Physiol.*, vol. 287, no. 1, pp. H302–310, Jul. 2004.
- [26] "Matlab r2007b. Natick, Massachusetts: the mathworks inc.; 2007." .
- [27] W. S. Rasband, "Imagej, u. s. national institutes of health, bethesda, maryland, usa, 1997-2011."
- [28] "Matlab r2007b. Natick, Massachusetts. Image processing toolbox, the mathworks, inc.;2007".
- [29] S. Haitao, L. Ning, G. Lijun, G. Fei, and L. Cheng, "Fractal dimension analysis of MDCT images for quantifying the morphological changes of the pulmonary artery tree in patients with pulmonary hypertension," *Korean J Radiol*, vol. 12, no. 3, pp. 289–296, Jun. 2011.
- [30] T. Alkhalifah and S. Fomel, "Implementing the fast marching eikonal solver: spherical versus Cartesian coordinates," *Geophysical Prospecting*, vol. 49, no. 2, pp. 165–178, Mar. 2001.

BIOGRAPHICAL SKETCH

Ankit Salgia was born in India in 1988. He attended G.S. Institute of Technology and Science – Indore, India from August 2006 to June 2010, where he received his Bachelor of Engineering in biomedical engineering. He began his master's in biomedical engineering at the University of Florida, Gainesville, FL during fall of 2010. He has been working under the direction of Dr. Walter G. O'Dell since March 2010, pursuing his research in the field of medical image processing.